Determining the optimal communication channels of arbitrary optical systems using integrated photonic processors

SeyedMohammad SeyedinNavadeh[1], Maziyar Milanizadeh[1,2], Francesco Zanetto[1], Giorgio Ferrari[3], Marco Sampietro[1], Marc Sorel[4,5], David A.B. Miller[6], Andrea Melloni[1] and Francesco Morichetti[1*]

[1*]Department of Electronics, Information and Bioengineering, Politecnico di Milano, Via Ponzio 34/5, Milan, 20133, Italy.
[2]now with Advanced Electronics and Photonics Research Centre, National Research Council Canada, 1200 Montréal Rd, Ottawa, K1A 0R6, ON, Canada.
[3]Department of Physics, Politecnico di Milano, Piazza Leonardo da Vinci 32, Milan, 20133, Italy.
[4]School of Engineering, University of Glasgow, Glasgow, G12 8QQ, UK.
[5]TeCIP Institute, Scuola Superiore Sant'Anna, Pisa, 56124, Italy.
[6]Ginzton Laboratory, Stanford University, 348 Via Pueblo, Stanford, 94305, CA, United States.

*Corresponding author(s). E-mail(s): francesco.morichetti@polimi.it;
Contributing authors: seyedmohammad.seyedinnavadeh@polimi.it; maziyar.milanizadeh@nrc-cnrc.gc.ca; francesco.zanetto@polimi.it; giorgio.ferrari@polimi.it; marco.sampietro@polimi.it; Marc.Sorel@glasgow.ac.uk; dabm@stanford.edu; andrea.melloni@polimi.it;

Abstract

Modes of propagation through an optical system are generally defined as the eigensolutions of the wave equation in the system. When propagation occurs through complicated or highly scattering media, however, modes are better identified as the best orthogonal communication channels to send information between sets of input and output apertures. Here, we determine the optimal bidirectional orthogonal communication channels through arbitrary and scattering optical systems using photonic processors. The processors consist of meshes of electrically tuneable Mach-Zehnder interferometers in silicon photonics. The meshes can configure themselves based on simple power maximization or minimization algorithms, without external calculations or calibration or any prior knowledge of the optical system. The identification of the communication mode channels corresponds to a singular-value decomposition of the entire optical system, autonomously performed by the photonic processors. We observe cross-talk below -30 dB between the optimized channels even in the presence of distorting masks or partial obstructions. In these cases, although the beams bear little resemblance to conventional mode families, they still show orthogonality. These findings offer potential for applications in multi-mode optical communication systems, promising efficient channel identification, adaptability to dynamic media, and robustness against environmental challenges.

Introduction

Finding the most efficient way to send information through a physical medium that is not well characterized, time-varying, or in some cases is even completely unknown, is a common problem in many different applications. Some examples include communications through turbulent systems [1, 2] or multi-mode optical fibers [3], imaging through scattering media [4, 5] or tissue [6], remote sensing [7], and beam shaping for localization and positioning [8]. In all these cases information is carried by electromagnetic waves and the problem translates into identifying which waves can best propagate through the medium. Structural imperfections, material inhomogeneities, and obstacles cause scattering and local distortions of the wavefront [9], resulting in deviations of the wave trajectory, end-to-end power loss, and mixing or cross-talk among the waves or channels that co-propagate through the medium [10, 11].

As shown in the generic scheme of Fig. 1a, any linear electromagnetic system with M input apertures and N output apertures can be described by an $N \times M$ matrix $\mathbf{M_c}$. This matrix depends both on the optical properties of the medium and on the number and position of the apertures. The waves that experience the lowest end-to-end loss between these sets of apertures, and which also are not subject to mutual mixing, correspond to the "communication modes" of the system [12, 13]. If $\mathbf{M_c}$ is known apriori in some way, these eigen-solutions can be readily obtained by calculating the singular value decomposition (SVD) of $\mathbf{M_c}$. SVD gives the set of orthogonal inputs that couple, one by one, to orthogonal outputs, giving independent communication channels. However, in many practical situations, $\mathbf{M_c}$ is not known so these solutions cannot be calculated mathematically.

In this work, we experimentally show that the best set of orthogonal waves that can propagate through arbitrary unknown optical media can be automatically found by using a pair of programmable photonic processors consisting of self-configuring meshes of Mach-Zehnder interferometers (MZIs), verifying a theoretical prediction of such a possibility [14]. MZI mesh architectures have been extensively used in previous works to "synthetize" arbitrary non-unitary matrices by implementing on-chip SVD [15, 16], with powerful demonstrations in computing systems based on photonic vector-matrix multiplication [17, 18], photonic accelerators [19], cryptography [20], photonic neural networks [21–24], photonic analog processors and equation solvers [25], and quantum photonic processors [26].

Here, instead, we use a pair of MZI architectures - one as transmitter, one as receiver - to "analyze" an unknown medium and find the elements of its SVD factorization [14]; at the same time, this process physically sets up the orthogonal channels or communication modes, which are the best coupled and lowest cross-talk channels through the medium or optical system, no matter what that medium or optical system is.

Specifically, we use programmable meshes of integrated MZIs coupled to arrays of surface gratings, capable of generating [27, 28], detecting [28, 29] and spatially resolving [30] complex optical beams with arbitrary shapes. The computation of the mesh settings for these waves is performed physically in-situ by only using power minimization or maximization algorithms, without any need for pre-calibration of the mesh elements, any knowledge of the media, or any external computation. We also show that the resulting vectors of input and output amplitudes experimentally correspond well to the theoretical optimal orthogonal SVD communication mode channels when the optical system is known and can be treated mathematically.

Results

Communication modes of an optical system

In the optical system of Fig. 1a, the "left" and "right" finite apertures define where the electromagnetic field is coupled and sampled, and they set discrete source and receiver vector spaces. The coupling between these sets of apertures can be described by a finite set of discrete bases consisting of M and N elements, respectively. Because of the beam divergence in an unconstrained volume, as well as diffraction and scattering due to the presence of obstacles in the free-space path, and also coupling loss between the optical beam and apertures, the matrix $\mathbf{M}_{\mathbf{c}[N\times M]}$ is generally non-unitary. Nonetheless, any matrix can be factorized according to the SVD as $\mathbf{M_c} = \mathbf{V\Sigma U}^\dagger$, where $\mathbf{U}_{[M\times M]}$ and $\mathbf{V}_{[N\times N]}$ are unitary matrices made from the left and right singular vectors $|\psi_{\mathbf{u}_m}\rangle$ and $|\phi_{\mathbf{v}_n}\rangle$, with $m = \{1,\ldots,M\}$ and $n = \{1,\ldots,N\}$ as their columns, respectively (see Methods). The orthonormal basis sets $\{|\psi_{\mathbf{u}_m}\rangle\}_{m=1}^{M}$ and $\{|\phi_{\mathbf{v}_n}\rangle\}_{n=1}^{N}$ represent the "communication mode pairs" of the system [12]. These orthogonal communication modes provide the field complex amplitudes, which maximize the power coupling between the source and receiving apertures, where the (power) coupling strengths associated with each mode pair are provided by the squared absolute value of the singular values $|\sigma_k|^2, k = \{1,\ldots,r = \operatorname{rank}\mathbf{M_c} \leq \min(M,N)\}$.

To give an example, we first simulate the case of two identical sets of $M = N = 9$ optical apertures (sources and receivers), which are positioned on two parallel planes according to a 3×3 square array configuration. We assume that the spacing between the apertures of each array is about 32λ, where $\lambda = 1550$ nm is the working optical wavelength, and that the two aperture planes are separated by a homogeneous medium (free space). The numerical solution to the SVD problem is shown in Fig. 1d for the first 3 modes with the highest coupling strengths. The different panels show the calculated far fields $\Psi_{\mathbf{u}_k}(el, az),\ k = \{1, 2, 3\}$ as a function of elevation (el) and azimuth (az) angles that are radiated by the left array of apertures when they are excited with the complex amplitudes of the left singular vectors $|\psi_{\mathbf{u}_k}\rangle$ (Note that capital letters $\Psi_{\mathbf{u}_k}$ and $\Phi_{\mathbf{v}_k}$ are used to indicate the far fields of the left and right singular vectors). The normalized coupling strengths $|\sigma_k|^2$ for all the 9 possible orthogonal communication modes are shown in decreasing order in Fig. 1e. Note that the 2nd and 3rd communication modes are degenerate ($\Psi_{\mathbf{u}_2}$ and $\Psi_{\mathbf{u}_3}$ have the same shape, just rotated by 90°) with the same magnitude of their singular values $|\sigma_2| = |\sigma_3|$, providing the same coupling efficiency between the two aperture planes.

Experimental results

Now, we experimentally demonstrate that by using a pair of photonic integrated processors these orthogonal modes can be found automatically. As shown in Fig. 1b, each processor consists of a mesh of tuneable MZIs that are connected respectively to M and N optical apertures on the left-hand and right-hand side of the optical medium. The number of MZI diagonals, $\hat{M}$ and $\hat{N}$ for the left and right processor, respectively, identifies the number of modes the system can support and find, i.e., $\min(\hat{M}, \hat{N})$. The two photonic processors used in this work are identical, with $\hat{M} = \hat{N} = 2$ as shown in the micrograph of Fig. 1c, each diagonal enabling the processor to generate or collect a mode of the system [15]. Two integrated thermo-optic phase shifters independently set the relative phase shift between the two input waveguides and between the inner arms of each MZI, providing the desired functionality in the MZIs (see Methods for more details on the design and technology of the photonic chip).

Two input ($I_{1,2}$) / output ($O_{1,2}$) waveguides are employed for coupling the light to standard single-mode optical fibers.

To automatically find the communication modes of the system, the MZI diagonal lines are controlled using a self-configuring algorithm aiming at maximizing the optical power at the output ports O_1 and O_2 when the light is injected at input ports I_1 and I_2, respectively [14, 15, 31]. A step-by-step description of the operating procedure is given in the Methods, while the mathematical treatment is reported in Supplementary Sec. 1. The electronics employed to implement the automated control system are described in the Methods and in Supplementary Sec. 2. When the system converges to the final state, the cross-power coupling for $I_1 \rightarrow O_2$ and $I_2 \rightarrow O_1$ is minimized, meaning that the two orthogonal communication modes of the system are excited. In these conditions, the unitary processor on the left generates the best estimation of the first two left-singular vectors $|\hat{\psi}_{\mathbf{u}_m}\rangle, m = \{1, 2\}$, and the processor on the right collects the first two right-singular vectors $|\hat{\phi}_{\mathbf{v}_n}\rangle, n = \{1, 2\}$. Thus, the end-to-end transmission ($I_{1,2} \rightarrow O_{1,2}$) can be described by the matrix see Methods)

$$\hat{\mathbf{\Sigma}} = \begin{bmatrix} \sigma_{11} & \sigma_{12} \\ \sigma_{21} & \sigma_{22} \end{bmatrix} \tag{1}$$

where σ_{11} and σ_{22} are the estimated singular values of the first two eigenmodes (which are the most strongly coupled channels), while the off-diagonal terms σ_{12} and σ_{21} indicate any remaining cross-talk between these channels.

Figure 1f shows the measured far-field beam shapes $\Psi_{\hat{\mathbf{u}}_k}, k = \{1, 2, 3\}$ once the automated self-alignment of the two processors is completed. Both the beam shapes and the power coupling strengths [$|\sigma_{ij}|^2,\ i = j$ in Fig. 1g] agree very well with the results obtained from the SVD computation of the first two communication modes shown in Fig. 1d. A numerical simulation of the beam-shape evolution during the self-configuration of the two-mesh system is shown in Supplementary Fig. 1c, confirming the agreement of the experimental solutions found at the convergence.

Interestingly, if the automated re-configuration procedure of the two processors is restarted, the shape of the first eigenmode always converges to the Gaussian-like shape of $\Psi_{\hat{\mathbf{u}}_1}$, while the second strongly-coupled mode may appear with the shape of $\Psi_{\hat{\mathbf{u}}_2}$, or $\Psi_{\hat{\mathbf{u}}_3}$, or with a combination of the two $\Psi_{\hat{\mathbf{u}}_{2+3}}$ (see Supplementary Movie 1). This ambiguity is to be expected for degenerate eigenmodes. Nonetheless, as shown in Fig. 1g, the end-to-end coupled power in all these cases (pink bars) is almost the same, confirming the degeneracy of these two modes. Figure 1h shows that the cross-coupling between all the pairs of orthogonal eigenmodes is lower than -30 dB, i.e., the off-diagonal terms of the $\hat{\mathbf{\Sigma}}$ matrix are negligible (loss analysis of the chip-to-chip system is provided in Methods). This result confirms that the two-processor system automatically implements optical SVD in-situ for the first two communications modes of the coupling matrix $\mathbf{M_c}$. The left and right singular matrices $\mathbf{U}$ and $\mathbf{V}$ are therefore correctly estimated by the two processors for these two communication modes and are embedded in the settings of the diagonal lines of MZIs.

Arbitrary sets of optical apertures. In the system considered so far, due to the symmetry of the left and right array apertures the shapes of the first and second modes resemble (in each diffraction order) the shapes of the first and second Hermite-Gaussian (HG) modes. This property is not, however, maintained in situations with aperture arrays with arbitrary sizes or shapes on either side. Optimum orthogonal communication mode channels still exist in such cases, but we should have no expectation that such HG-like shapes are then associated with them.

In the case of left and right arrays with a different number of apertures, the coupling matrix $\mathbf{M_c}$ is no longer square ($M \neq N$). To emulate this condition experimentally, we used the same optical setup as in Fig. 1b, but we intentionally switched off selected subsets of apertures on both sides by “freezing” an MZI in the chain in its “bar” state, optically disconnecting any further MZIs from the processor [Fig. 2a]. The automated configuration algorithm of the two-processor system is applied to control only the field radiated and received by the apertures that are operative. This means that in each considered case, the system is forced to use different discrete basis functions to describe the field at the aperture planes.

In the following two different cases are considered: (i) Fig. 2b shows the case of a non-symmetric system where on one side the number of “ON” apertures in use is kept constant ($N = 9$ on the right side) and on the other side is progressively reduced ($M = 9, 8, \ldots, 4$); while (ii) Fig. 2c refers to a system with the same number of apertures in use ($M = N$) progressively reduced from 9 to 4 according to a (point-)symmetric configuration (as shown in the Extended Data Fig. 1). The bar charts in both panels show the singular values σ_{11} (blue) and σ_{22} (pink) of the first two most strongly coupled modes (normalized to the reference case of $M = N = 9$ shown in the leftmost bar) versus the number of apertures ON. In agreement with numerical simulations (see Extended Data Fig. 2 for comparison with simulations), for both modes, though the coupling strength reduces with the number of OFF-state apertures, the coupling efficiency of the first mode remains about twice that of the second mode. Notably, though, in all the cases, the cross-talk between modes, which is given by σ_{12} (cyan) and σ_{21} (orange), remains below -30 dB, confirming the mutual orthogonality of the established solutions.

The beam shapes for some example cases are shown in Fig. 2d. For the symmetric case of $M = N$ the same far-field shapes are obtained for the left $\Psi_{\hat{\mathbf{u}}_{1,2}}$ and right $\Phi_{\hat{\mathbf{v}}_{1,2}}$ modes, while for the non-symmetric case $M \neq N$ different far-field shapes are observed since the left and right mode pairs are defined on different discrete spaces (see Extended Data Fig. 1 for a complete set of beam shapes). In any case, the reduction of the dimensionality of the aperture arrays breaks the original symmetry of the 3×3 square arrays and the best-coupled modes do not even approximately resemble any of the conventional families of modes typically considered in free-space optics (e.g., Hermite-Gauss, Laguerre-Gauss, etc.).

Beaming through obstacles. Theoretically, SVD predicts that orthogonal modes do always exist, whatever the coupling matrix $\mathbf{M_c}$ [12]. This means that they can be found even in the presence of arbitrary obstacles or strongly scattering media between the aperture planes. To demonstrate this, we introduce different types of obstacles in the optical path (at the far-field plane in Fig. 1b) that partially obstruct and perturb the propagation of the optical field. Figure 3 shows a selection of obstacles, consisting of amplitude masks, which are patterned with the shape of periodic circular spots (Fig. 3a), where the period is the same as the diffraction orders in the far-field plane to maximize the impact, and with a non-periodic shape (Fig. 3b), and a phase-only aberrator emulated by using a spatial light modulator (SLM) (Fig. 3c). After inserting the masks, the two processors self-configure to find the best end-to-end power couplings $I_1 \rightarrow O_1$ and $I_2 \rightarrow O_2$. As expected, the far-field shapes $\Psi_{\hat{\mathbf{u}}_1}$ and $\Psi_{\hat{\mathbf{u}}_2}$ that result after the processors establish the best chip-to-chip communication through different obstacles do not correspond to any standard mode sets (e.g., Hermite-Gaussian), yet they are still mutually orthogonal. The orthogonality between these modes is confirmed by the very low cross-talk ($\sigma_{ij},\ i \neq j$) shown in the bar charts of Fig. 3, and the singular values ($\sigma_{ij}, i = j$) are only slightly reduced with respect to the reference case (no mask). Extended Data Fig. 3 shows other cases with different mask shapes and corresponding beam shapes and cross-talks between orthogonal channels.

Data communication experiment. The two-processor system was employed to perform a data communication experiment between the two chips. Figure 4 shows the eye diagrams and the bit-error ratio (BER) of two intensity-modulated on-off keying (OOK) signals at a data rate of 5 Gbps, which are injected at input ports I_1 and I_2 of the first chip and extracted at output ports O_1 and O_2 of the second chip. The quality of the signals simultaneously transmitted by using the modes determined by the processors (Fig. 4a, two channels) is comparable with the quality of the signals that are transmitted individually (Fig. 4a, single channel). The presence of an obstacle breaks such orthogonality, introducing mutual optical cross-talk and deteriorating the transmission performance (Fig. 4b); however, the two-processor system can find the pair of optimal communication channels that remain orthogonal through such obstacle, recovering the reference BER performance (Fig. 4c).

Discussion

We demonstrated the automatic finding of orthogonal communication modes between arbitrary sets of optical apertures at both ends of a free-space optical system. The effective computation of these modes is performed physically through a pair of programmable photonic processors made of self-configuring MZIs, without any knowledge of the optical system in between and without any need for calibration of the processor elements. Essentially no cross-talk between mode pairs (experimentally better than -30 dB) is obtained even when the number and configuration of the optical apertures at the two ends are different, and even when amplitude obstructions and/or phase perturbations are introduced in the free-space medium.

In all cases that can readily also be simulated, these beams experimentally correspond well to the theoretical optimal orthogonal communication mode channels, which can be calculated mathematically using SVD. Especially in cases with obstructions or different aperture sets on the two ends, these optimal modes may have little or no similarity to standard mode families, but nonetheless, they show the low cross-talk associated with orthogonality. Mathematically, only these SVD channels or communication modes both maximize power transmission and are orthogonal [12].

In this work, these concepts are experimentally validated by using photonic processors with two diagonal lines of MZIs connected to 9 input/output integrated apertures (grating couplers), which are used to find the first two orthogonal modes of several different free-space optical systems; however, this approach is scalable to more than two modes by using mesh architectures with a larger number of optical inputs and outputs and more MZI diagonal lines [18] (see Methods). Once the optical apertures in the source and receiving volume are set, all the communication modes between them are found sequentially starting from the one with the strongest singular value (best-coupled mode) down to the ones with progressively lower singular values (less strongly-coupled modes). Modes with closely spaced singular values (i.e., quasi-degenerate modes) are more sensitive to any perturbation of the system. Therefore, the order according to which quasi-degenerate modes are found can be modified by small changes in the system, and this is what actually happens to modes $\Psi_{\hat{\mathbf{u}}_2}$ and $\Psi_{\hat{\mathbf{u}}_3}$ in the experiment of Fig. 1f. Nonetheless, the modes that are found are always guaranteed to be orthogonal, and they represent the two most strongly coupled modes in each case.

Within the operational wavelength range of the two-processor system (see Methods), multiple wavelength division multiplexed (WDM) channels, can be mapped onto the same communication mode. This means that wavelength can be used as another basis for scaling the number of channels, provided that the entire optical system (including obstacles, aberrators, etc.) equally affects all the wavelengths. Further, each mode can be individually established and adaptively optimized (for instance in dynamically varying media) without the need for switching off the other coexisting modes provided that each transmitted beam is labeled with a suitable pilot tone (see Supplementary Sec. 2) [32]

Although the examples reported in this work refer to forward-propagating modes only, once the free-space optical system is set (i.e., number and position of the input/output apertures, presence/absence of obstacles in between), due to the reciprocity of the system the same mode pairs are established for forward and backward propagation. Also, the presented results can be straightforwardly generalized to the case of chips that do not remain fixed in space, because the two-processor system allows us also to send and receive optical beams along different directions [27, 29].

The proposed system could be also used to find the guided modes in a multi-mode optical fiber that exhibit the highest end-to-end mutual isolation also in the presence of bending, deformation, and structural defects [3]. Since photonic processors preserve the phase information encoded in the optical signals, our approach applies also to coherent transmission systems with arbitrary amplitude and phase modulation formats as well as to spatial division multiplexing (SDM) systems to handle signal orthogonalization directly in the optical domain [33], and does not require any digital signal processing at the data rate to make such orthogonalization. Finally, the reconfiguration time of photonic processors realized on a silicon photonic platform, which is faster than 10 μs in the case of thermal actuators [34] and in the sub-ns range for electro-optic actuators [35], should also allow real-time adaptation [36] of the optimal modes to time-varying media, such as turbulent environments, potentially as fast as or faster than available wave-front shapers [37].

Acknowledgments

S.S., G.F., M.Sampietro, M.Sorel, A.M. and F.M. acknowledge support by the European Commission under the Horizon 2020 Programme (SuperPixels, grant no. 829116). S.S., M.Sorel, A.M. and F.M. acknowledge support from the Italian National Recovery and Resilience Plan (NRRP) of NextGenerationEU, partnership on "Telecommunications of the Future" (PE00000001 - program "RESTART", Structural Project "Rigoletto" and Focused Project "HePIC"). D.A.B.M. acknowledges support by the Air Force Office of Scientific Research (AFOSR, grants FA9550-17-1-0002 and FA9550-21-1-0312). Part of this work was carried out at Polifab, the micro- and nanofabrication facility of Politecnico di Milano (https://www.polifab.polimi.it/). We thank C. De Vita for his support in the realization of the phase masks used in the experiments and V. Grimaldi for his support in the development of the control electronics.

Author contributions

M.M. and S.S. designed the photonic chips and performed the optical measurements. F.Z., G.F., and M.Sampietro developed electronic control systems. M.Sorel contributed to the design of the photonic chip. S.S., M.M., A.M., D.A.B.M., and F.M. conceived the experiments and analyzed the experimental data. S.S., D.A.B.M., and F.M. wrote the manuscript. All the authors contributed to the revision of the manuscript. F.M. supervised the project.

Competing interests

The authors declare no competing interests

Figure Captions

Figure 1

Finding best orthogonal communication modes automatically with a pair of photonic integrated processors. **a**, Schematic of a generic optical system with M input and N output optical apertures in source and receiving volumes, respectively, which can be defined by a coupling matrix $\mathbf{M_c}$. **b**, Two programmable photonic integrated processors made of tuneable beam splitters connected to M (left-hand side) and N (right-hand side) optical apertures are used to automatically find pairs of orthogonal communication modes through arbitrary optical media. $I_{1,2} and O_{1,2}$ are the input and output ports of the processor, respectively, which define end-to-end power coupling and cross-talk between two established channels. **c**, Top-view microphotograph of the silicon photonic chip hosting 9 optical apertures (3×3 square array of grating couplers) connected to a two-diagonal mesh of thermally-tuneable MZIs. **d**, **f**, Far-field shapes of the first 3 modes that provide the highest coupling strengths between two symmetric sets of apertures ($M = N = 9$), as obtained in **d** numerically by computing the SVD of the system ($\Psi_{\mathbf{u}_k},\ k = \{1, 2, 3\}$), and in **f** experimentally by finding them using a two-processor system ($\Psi_{\hat{\mathbf{u}}_k},\ k = \{1, 2, 3\}$). Panels **e** (simulation, all 9 modes) and

g (experiment, first 2 modes) show the coupling strengths ($\sigma_{ij},\ i = j$) normalized to the first mode. Orthogonality between the different communication modes ($\sigma_{ij},\ i \neq j$) is experimentally demonstrated by the low cross coupling (< -30 dB) in panel **h**. The error bar in the bar charts is about $\pm$ 1 dB for the optical cross-talk and less than 0.1 dB (about 2%) for the coupling strength.

Figure 2

Orthogonal modes between arbitrary sets of optical apertures. a, The number of input M / output N optical apertures in the source/receiving volume can be modified by controlling the corresponding MZIs of the mesh processors. Panels **b** and **c** show the measured input/output coupling strengths σ_{11} and σ_{22} of the first two modes (normalized to that of the first mode when $M = N = 9$) when the number of apertures is reduced according to a non-symmetric (panel **b**, $M = 9, 8, ..., 4;\ N = 9$) or (point-)symmetric configuration (panel **c**, $M = N = 9, 8, ..., 4$). A high degree of orthogonality between the first two modes (cross-talk < -30 dB, as shown by σ_{12} and σ_{21} bars) is experimentally achieved in both cases [see Extended Data Fig. 2 for comparison with simulations]. Selected far-field beam shapes of the left and right modes are shown in **d** for a symmetric case ($M = N = 9$) and a non-symmetric case ($M = 5, N = 9$) [See Extended Data Fig. 1 for complete set of beam shapes]. Error bars as in Fig. 1.

Figure 3

Orthogonal modes through obstacles and scattering media. The two-processor system is used to find pairs of orthogonal optical beams propagating through different kinds of obstacles; **a**, periodic pattern of circular metal obstructions, **b**, micro-scale reproduction of the Politecnico di Milano logo, and **c**, phase-only aberrator. The far-field beam shapes providing maximum coupling strengths and minimum mutual cross-talk are shown. The four bars represent $\sigma_{ij}, i, j = \{1, 2\}$ normalized to the power of the first mode without obstacle in dB scale, all starting from zero. For those scatterers with a periodic pattern, the periodicity of the scatterers matches the periodicity of the diffraction orders of the beam in the scatterer plane. The peak-to-peak phase shift introduced by the phase-only aberrator is 2π. Error bars as in Fig. 1.

Figure 4

Orthogonality between data communication channels. The performances of the two-processor system are assessed by transmitting two intensity-modulated NRZ-OOK signals at 5 Gbps. **a**, Eye diagrams and BER of the reference channels that are individually transmitted (only a single channel is switched on) through the system in the absence of any obstacle; when the interfering channel is switched on (two channels), no significant degradation is observed in the quality of the received signals. **b**, Insertion of an obstacle (specifically the donuts-like mask of Extended Fig. 3c is used here) breaks the orthogonality between the communication modes causing strong channel interference and signal degradation. **c**, The reconfiguration of the two-processor system enables the establishment of a new pair of orthogonal modes that can be transmitted through the obstacle with negligible mutual crosstalk.

References

[1] Cox, M.A., Mphuthi, N., Nape, I., Mashaba, N., Cheng, L., Forbes, A.: Structured light in turbulence. IEEE Journal of Selected Topics in Quantum Electronics **27**(2), 1–21 (2021). https://doi.org/10.1109/JSTQE.2020.3023790

[2] Hill, R.J.: Optical propagation in turbulent water. J. Opt. Soc. Am. **68**(8), 1067–1072 (1978). https://doi.org/10.1364/JOSA.68.001067

[3] Matthès, M.W., Bromberg, Y., de Rosny, J., Popoff, S.M.: Learning and avoiding disorder in multimode fibers. Phys. Rev. X **11**, 021060 (2021). https://doi.org/10.1103/PhysRevX.11.021060

[4] Vellekoop, I.M., Mosk, A.P.: Focusing coherent light through opaque strongly scattering media. Opt. Lett. **32**(16), 2309–2311 (2007). https://doi.org/10.1364/OL.32.002309

[5] Yoon, S., Kim, M., Jang, M., Choi, Y., Choi, W., Kang, S., Choi, W.: Deep optical imaging within complex scattering media. Nature Reviews Physics **2**(3), 141–158 (2020). https://doi.org/10.1038/s42254-019-0143-2

[6] Biton, N., Kupferman, J., Arnon, S.: Oam light propagation through tissue. Scientific Reports **11**(1), 2407 (2021). https://doi.org/10.1038/s41598-021-82033-6

[7] Ishimaru, A.: In: Strohbehn, J.W. (ed.) The beam wave case and remote sensing, pp. 129–170. Springer, Berlin, Heidelberg (1978). https://doi.org/10.1007/3540088121_19

[8] Heck, M.J.R.: Highly integrated optical phased arrays: photonic integrated circuits for optical beam shaping and beam steering. Nanophotonics **6**(1), 93–107 (2017). https://doi.org/10.1515/nanoph-2015-0152

[9] Nape, I., Singh, K., Klug, A., Buono, W., Rosales-Guzman, C., McWilliam, S. Amy Franke-Arnold, Kritzinger, A., Forbes, A. Patricia Dudley, Forbes, A.: Revealing the invariance of vectorial structured light in complex media. Nature Photonics **16**(7), 538–546 (2022). https://doi.org/10.1038/s41566-022-01023-w

[10] Churnside, J.H., Lataitis, R.J.: Wander of an optical beam in the turbulent atmosphere. Appl. Opt. **29**(7), 926–930 (1990). https://doi.org/10.1364/AO.29.000926

[11] Gong, L., Zhao, Q., Zhang, H., Hu, X.-Y., Huang, K., Yang, J.-M., Li, Y.-M.: Optical orbital-angular-momentum-multiplexed data transmission under high scattering. Light: Science & Applications **8**, 27 (2019). https://doi.org/10.1038/s41377-019-0140-3

[12] Miller, D.A.B.: Waves, modes, communications, and optics: a tutorial. Adv. Opt. Photon. **11**(3), 679–825 (2019). https://doi.org/10.1364/AOP.11.000679

[13] Miller, D.A.B.: Communicating with waves between volumes: evaluating orthogonal spatial channels and limits on coupling strengths. Appl. Opt. **39**(11), 1681–1699 (2000). https://doi.org/10.1364/AO.39.001681

[14] Miller, D.A.B.: Establishing optimal wave communication channels automatically. J. Lightwave Technol. **31**(24), 3987–3994 (2013)

[15] Miller, D.A.B.: Self-configuring universal linear optical component. Photon. Res. **1**(1), 1–15 (2013). https://doi.org/10.1364/PRJ.1.000001

[16] Harris, N.C., Carolan, J., Bunandar, D., Prabhu, M., Hochberg, M., Baehr-Jones, T., Fanto, M.L., Smith, A.M., Tison, C.C., Alsing, P.M., Englund, D.: Linear programmable nanophotonic processors. Optica **5**(12), 1623–1631 (2018). https://doi.org/10.1364/OPTICA.5.001623

[17] Zhou, H., Zhao, Y., Xu, G., Wang, X., Tan, Z., Dong, J., Zhang, X.: Chip-scale optical matrix computation for pagerank algorithm. IEEE Journal of Selected Topics in Quantum Electronics **26**(2), 1–10 (2020). https://doi.org/10.1109/JSTQE.2019.2943347

[18] Bogaerts, W., Pérez, D., Capmany, J., Miller, D.A.B., Poon, J., Englund, D., Morichetti, F., Melloni, A.: Programmable photonic circuits. Nature **586**(7828), 207–216 (2020). https://doi.org/10.1038/s41586-020-2764-0

[19] Zhou, H., Dong, J., Cheng, J., Dong, W., Huang, C., Shen, Y., Zhang, Q., Gu, M., Qian, C., Chen, H., Ruan, Z., Zhang, X.: Photonic matrix multiplication lights up photonic accelerator and beyond. Light: Science & Applications **11**(30) (2022). https://doi.org/10.1038/s41377-022-00717-8

[20] Pai, S., Park, T., Ball, M., Penkovsky, B., Dubrovsky, M., Abebe, N., Milanizadeh, M., Morichetti, F., Melloni, A., Fan, S., Solgaard, O., Miller, D.A.B.: Experimental evaluation of digitally verifiable photonic computing for blockchain and cryptocurrency. Optica **10**(5), 552–560 (2023). https://doi.org/10.1364/OPTICA.476173

[21] Shen, Y., Harris, N.C., Skirlo, S., Prabhu, M., Baehr-Jones, T., Hochberg, M., Sun, X., Zhao, S., Larochelle, H., Englund, D., Soljačić, M.P.: Deep

learning with coherent nanophotonic circuits. Nature Photonics **11**(7), 441–446 (2017). https://doi.org/10.1038/nphoton.2017.93

[22] Shokraneh, F., Geoffroy-gagnon, S., Liboiron-Ladouceur, O.: The diamond mesh, a phase-error- and loss-tolerant field-programmable mzi-based optical processor for optical neural networks. Opt. Express **28**(16), 23495–23508 (2020). https://doi.org/10.1364/OE.395441

[23] Tian, Y., Zhao, Y., Liu, S., Li, Q., Wang, W., Feng, J., Guo, J.: Scalable and compact photonic neural chip with low learning-capability-loss. Nanophotonics **11**(2), 329–344 (2022). https://doi.org/10.1515/nanoph-2021-0521

[24] Pai, S., Sun, Z., Hughes, T.W., Park, T., Bartlett, B., Williamson, I.A.D., Minkov, M., Milanizadeh, M., Abebe, N., Morichetti, F., Melloni, A., Fan, S., Solgaard, O., Miller, D.A.B.: Experimentally realized in situ backpropagation for deep learning in photonic neural networks. Science **380**(6643), 398–404 (2023). https://doi.org/10.1126/science.ade8450

[25] Tzarouchis, D.C., Mencagli, M.J., Edwards, B., Engheta, N.: Mathematical operations and equation solving with reconfigurable metadevices. Light: Science & Applications **11**(263) (2022). https://doi.org/10.1038/s41377-022-00950-1

[26] Harris, N.C., Steinbrecher, G.R., Prabhu, M., Lahini, Y., Mower, J., Bunandar, D., Chen, C., Wong, F.N.C., Baehr-Jones, T., Hochberg, M., Lloyd, S., Englund, D.: Quantum transport simulations in a programmable nanophotonic processor. Nature Photonics **11**(7), 447–452 (2017). https://doi.org/10.1038/nphoton.2017.935

[27] Milanizadeh, M., Toso, F., Ferrari, G., Jonuzi, T., Miller, D.A.B., Melloni, A., Morichetti, F.: Coherent self-control of free-space optical beams with integrated silicon photonic meshes. Photon. Res. **9**(11), 2196–2204 (2021). https://doi.org/10.1364/PRJ.428680

[28] Miller, D.A.B.: Analyzing and generating multimode optical fields using self-configuring networks. Optica **7**(7), 794–801 (2020). https://doi.org/10.1364/OPTICA.391592

[29] Milanizadeh, M., SeyedinNavadeh, S., Zanetto, F., Grimaldi, V., Vita, C.D., Klitis, C., Sorel, M., Ferrari, G., Miller, D.A.B., Melloni, A., Morichetti, F.: Separating arbitrary free-space beams with an integrated photonic processor. Light: Science & Applications **11**, 197 (2022). https://doi.org/10.1038/s41377-022-00884-8

[30] Bütow, J., Eismann, J.S., Milanizadeh, M., Morichetti, F., Melloni, A., Miller, D.A.B., Banzer, P.: Spatially resolving amplitude and phase of light with a reconfigurable photonic integrated circuit. Optica **9**(8), 939–946 (2022). https://doi.org/10.1364/OPTICA.458727

[31] Miller, D.A.B.: Self-aligning universal beam coupler. Opt. Express **21**(5), 6360–6370 (2013). https://doi.org/10.1364/OE.21.006360

[32] Annoni, A., Guglielmi, E., Carminati, M., Ferrari, G., Sampietro, M., Miller, D.A., Melloni, A., Morichetti, F.: Unscrambling light—automatically undoing strong mixing between modes. Light: Science & Applications 2017 6:12 **6**, 17110–17110 (2017). https://doi.org/10.1038/lsa.2017.110

[33] Fontaine, N. K., Doerr, C.R., Mestre, M. A, Ryf, R., Winzer, P.J., Buhl,

L.L., Sun, Y.: Jiang, X.: Lingle, R.: Space-division multiplexing and all-optical MIMO demultiplexing using a photonic integrated circuit. Proc. OFC/NFOEC, Los Angeles, CA, USA, 1–3 (2012). https://doi.org/10.1364/NFOEC.2012.PDP5B.1

[34] Harris, N.C., Ma, Y., Mower, J., Baehr-Jones, T., Englund, D., Hochberg, M., Galland, C.: Efficient, compact and low loss thermo-optic phase shifter in silicon. Opt. Express **22**(9), 10487–10493 (2014). https://doi.org/10.1364/OE.22.010487

[35] Rahim, A., Hermans, A., Wohlfeil, B., Petousi, D., Kuyken, B., Thourhout, D.V., Baets, R.G.: Taking silicon photonics modulators to a higher performance level: state-of-the-art and a review of new technologies. Advanced Photonics **3**(2), 024003 (2021). https://doi.org/10.1117/1.AP.3.2.024003

[36] Choutagunta, K., Roberts, I., Miller, D.A.B., Kahn, J.M.: Adapting mach–zehnder mesh equalizers in direct-detection mode-division-multiplexed links. Journal of Lightwave Technology **38**(4), 723–735 (2020). https://doi.org/10.1109/JLT.2019.2952060

[37] Tzang, O., Niv, E., Singh, S., Labouesse, S., Myatt, G., Piestun, R.: Wavefront shaping in complex media with a 350 khz modulator via a 1d-to-2d transform. Nature Photonics **13**(11), 788–793 (2019). https://doi.org/10.1038/s41566-019-0503-6

[38] Zanetto, F., Grimaldi, V., Toso, F., Guglielmi, E., Milanizadeh, M., Aguiar, D., Moralis-Pegios, M., Pitris, S., Alexoudi, T., Morichetti, F., Melloni, A., Ferrari, G., Sampietro, M.: Dithering-based real-time control of cascaded silicon photonic devices by means of non-invasive detectors.

IET Optoelectronics **15**(2), 111–120 (2021). https://doi.org/10.1049/ote2.12019

[39] Xue, Y., Han, Y., Wang, Y., Li, J., Wang, J., Zhang, Z., Cai, X., Tsang, H.K., Lau, K.M.: High-speed and low dark current silicon-waveguide-coupled iii-v photodetectors selectively grown on soi. Optica **9**(11), 1219–1226 (2022). https://doi.org/10.1364/OPTICA.468129

[40] Fatemi, R., Khial, P.P., Khachaturian, A., Hajimiri, A.: Breaking fov-aperture trade-off with multi-mode nano-photonic antennas. IEEE Journal of Selected Topics in Quantum Electronics **27**(1), 1–14 (2021). https://doi.org/10.1109/JSTQE.2020.3026966

[41] Sacher, W.D., Huang, Y., Lo, G.-Q., Poon, J.K.S.: Multilayer silicon nitride-on-silicon integrated photonic platforms and devices. J. Lightwave Technol. **33**(4), 901–910 (2015). https://doi.org/10.1109/JLT.2015.2392784

[42] Milanizadeh, M., Aguiar, D., Melloni, A., Morichetti, F.: Canceling thermal cross-talk effects in photonic integrated circuits. Journal of Lightwave Technology **37**(4), 1325–1332 (2019). https://doi.org/10.1109/JLT.2019.2892512

[43] Zemtsov, D.S., Zhigunov, D.M., Kosolobov, S.S., Zemtsova, A.K., Puplauskis, M., Pshenichnyuk, I.A., Drachev, V.P.: Broadband silicon grating couplers with high efficiency and a robust design. Opt. Lett. **47**(13), 3339–3342 (2022). https://doi.org/10.1364/OL.457284

[44] Lu, Z., Yun, H., Wang, Y., Chen, Z., Zhang, F., Jaeger, N.A.F., Chrostowski, L.: Broadband silicon photonic directional coupler using

asymmetric-waveguide based phase control. Opt. Express **23**(3), 3795–3808 (2015). https://doi.org/10.1364/OE.23.003795

[45] Poulton, C.V., Byrd, M.J., Russo, P., Timurdogan, E., Khandaker, M., Vermeulen, D., Watts, M.R.: Long-Range LiDAR and Free-Space Data Communication With High-Performance Optical Phased Arrays. IEEE Journal of Selected Topics in Quantum Electronics **25**, 1–8 (2019). https://doi.org/10.1109/JSTQE.2019.2908555

Methods

SVD factorization of the optical system. In this section, we define the main parameters of the SVD factorization of the optical system we are considering. According to SVD theory, any matrix can be factorized as

$$\mathbf{M_c} = \mathbf{V\Sigma U}^\dagger = \\ = \begin{bmatrix} | & & | \\ |\phi_{\mathbf{v}_1}\rangle & \ldots & |\phi_{\mathbf{v}_N}\rangle \\ | & & | \end{bmatrix} \begin{bmatrix} \sigma_1 & & & \\ & \ddots & & 0 \\ & & \sigma_r & \\ & 0 & & \end{bmatrix} \begin{bmatrix} - & \langle\psi_{\mathbf{u}_1}| & - \\ & \vdots & \\ - & \langle\psi_{\mathbf{u}_M}| & - \end{bmatrix} \tag{2}$$

where the dagger † indicates Hermitian adjoint or conjugate transpose. (In this “Dirac” notation, $\langle\alpha|$, which can be viewed as a “row” vector, is the Hermitian adjoint of the “column” vector $|\alpha\rangle$.) $\mathbf{U}_{[M\times M]}$ and $\mathbf{V}_{[N\times N]}$ are unitary matrices made from the left and right singular vectors

$$|\psi_{\mathbf{u}_m}\rangle = \begin{bmatrix} u_{1m} \\ \vdots \\ u_{Mm} \end{bmatrix}, \quad |\phi_{\mathbf{v}_n}\rangle = \begin{bmatrix} v_{1n} \\ \vdots \\ v_{Nn} \end{bmatrix} \tag{3}$$

with $m = \{1,\ldots,M\}$ and $n = \{1,\ldots,N\}$ as their columns, respectively, and $\mathbf{\Sigma}_{[N\times M]}$ is a diagonal matrix with singular values $\sigma_k, k = \{1,\ldots,r = \operatorname{rank}\mathbf{M_c} \leq \min(M,N)\}$, arranged in descending order according to the magnitudes ($|\sigma_1| \geq |\sigma_2| \geq \ldots \geq |\sigma_r| > 0$) of its non-zero elements. Note that the choice of “left” and “right” is according to the schematic of the two sets of apertures in Fig. 1a, which is the opposite of the mathematical notation often used with SVD. The inputs $|\psi_{\mathbf{u}_k}\rangle$ and outputs $\sigma_k|\phi_{\mathbf{v}_k}\rangle$ are uniquely specified (at least within normalization and phase factors, and arbitrariness of degenerate solutions), and the orthonormal basis sets $\{|\psi_{\mathbf{u}_m}\rangle\}_{m=1}^{M}$ and $\{|\phi_{\mathbf{v}_n}\rangle\}_{n=1}^{N}$ represent the "communication mode pairs" of the system [12].

The sets of orthogonal input vectors $|\psi_{\mathbf{u}_k}\rangle$ that couple one-by-one to orthogonal output vectors $|\phi_{\mathbf{v}_k}\rangle$, with coupling strengths σ_k, always exist for any matrix, and hence such orthogonal channels always exist, no matter what the linear medium or optics is between the inputs and outputs [12, 13]. Note too that, in the communication modes approach [12], it is the pairs of vectors $|\psi_{\mathbf{u}_k}\rangle$ and $|\phi_{\mathbf{v}_k}\rangle$ that are the "modes" in the system. Each of these vectors is the solution of an eigen-problem; $|\psi_{\mathbf{u}_k}\rangle$ is an eigenvector of $\mathbf{M_c}^\dagger\mathbf{M_c}$, and $|\phi_{\mathbf{v}_k}\rangle$ of $\mathbf{M_c}\mathbf{M_c}^\dagger$ (with also the relation $\mathbf{M_c}|\psi_{\mathbf{u}_k}\rangle = \sigma_k|\phi_{\mathbf{v}_k}\rangle$). The electromagnetic field or beam between the inputs and outputs is not itself the mode, is not the solution of an eigen-problem, and, unlike many common families of "modes", does not necessarily retain its shape as it propagates [12].

Due to the symmetry of this specific system, the backward singular vectors $|\phi_{\mathbf{v}_k}\rangle$ from the right array of apertures would be complex conjugates (phase conjugates) of $|\psi_{\mathbf{u}_k}\rangle$, and therefore would have the same power far-field shapes. The two-processor system is used to estimate the singular values matrix $\mathbf{\Sigma}$ as

$$\hat{\mathbf{\Sigma}}_{[\hat{N}\times\hat{M}]} = \hat{\mathbf{V}}^\dagger_{[\hat{N}\times N]}(\mathbf{V}\mathbf{\Sigma}\mathbf{U}^\dagger)_{[N\times M]}\hat{\mathbf{U}}_{[M\times\hat{M}]} \tag{4}$$

where the processor on the left generates the best estimation of the left-singular vectors $|\hat{\psi}_{\mathbf{u}_m}\rangle, m = \{1,\ldots,\hat{M} \leq M\}$ which are the columns of $\hat{\mathbf{U}}$, and the processor on the right generates the right-singular vectors $|\hat{\phi}_{\mathbf{v}_n}\rangle, n = \{1,\ldots,\hat{N} \leq N\}$ which are the columns of $\hat{\mathbf{V}}$. The "hat" in the notation is used to indicate parameters that are estimated by the two-processor system. The consistency of our numerical and experimental results and their agreement with what we expect from SVD modeling (as well as the fundamental theory) are strong evidence that the two-processor system finds a very good approximation to the ideal SVD channels (or communication modes). Mode orthogonality is evaluated by measuring the end-to-end cross-talk, which is given by the ratio between the cross-coupling between different modes (off-diagonal terms $|\sigma_{ij}|^2$ of $\hat{\mathbf{\Sigma}}$, with $i \neq j$) and the power of the considered mode (diagonal terms $|\sigma_{ij}|^2$, with $i = j$).

Configuration algorithm. To understand how this system works, consider the architecture in Fig. 1b. Each photonic processor consists of two diagonal lines of MZIs. Suppose first we shine the light into the upper waveguide I_1 on the left and hence into the "first" (blue) diagonal line of MZIs in this processor. For the moment, we presume that the phase shifters in the MZIs are set in some arbitrary way. As a result, generally, some light will appear out of each of the 9 waveguides on the right of this left photonic processor. That light emerges from the gratings and passes into the optical system (characterized by some matrix $\mathbf{M_c}$). Some resulting light is then collected by the gratings at the inputs to the right photonic processor, and passes into the first (blue) diagonal line of MZIs in the right processor.

A key point is that this "blue" diagonal line in the photonic processor on the right can now function as a self-aligning beam coupler [31]. A simple progressive algorithm allows us to set all the MZIs in this diagonal line so that all the input power in all 9 waveguides is routed to the output waveguide O_1 at the upper right. Such an algorithm can work by progressively configuring each MZI, starting with the one at the bottom left of this row, so that no power from it passes into the second (pink) row; equivalently all the power in this MZI is routed to its upper output. We can then proceed similarly along the diagonal row of MZIs so all the power ends up in output waveguide O_1. We can run this algorithm based on signals from mostly-transparent photodetectors in the waveguides between the blue and pink rows [32], successively minimizing the powers in them, or we can run a version of this algorithm based only on maximizing the power in the output O_1 [31]. This second option was used in the experiments reported in this work. In particular, a dithering-based strategy was implemented to enable the simultaneous monitoring and control of several MZIs with a single external photodetector (see Methods, "Control Electronics").

This first self-aligning process has successfully coupled all the power collected by gratings on the right to output O_1, but it has not yet established the overall optimum channel through the whole system. To find this channel, we can proceed next by turning off the input power at port I_1, and instead shining power backwards into O_1. Then we similarly self-align the MZIs in the first (blue) line of MZIs in the left photonic processor to couple all this collected backwards power into waveguide I_1. If we then repeat this process alternately forwards and backwards, the whole system will converge to the best coupled channel, as shown mathematically in [14] (see also Supplementary Sec. 1). This process has therefore found the first, most strongly coupled communication mode of the entire system, essentially by a variational process.

Now, if we shine input power into the second waveguide I_2 in the left photonic processor, and hence into the second (pink) line of MZIs, that power will emerge from the gratings in that left processor, and some of it will be coupled through the optical system and the gratings in the right processor and into the waveguides and MZI lines in that processor. A key point is that, because we have set the "blue" lines of MZIs to implement the first communication mode, none of that power originally shone into I_2 will emerge from the upper waveguide O_1. This is guaranteed by the orthogonality of the communications modes and the unitarity of the processors (where we note that unitary processors preserve orthogonalities). Any input fields to the optical system that are orthogonal to the first communication mode input field will generate output fields that are orthogonal to the first communication mode's output field. Instead, the input power at port I_2 will all flow into the second (pink) line of MZIs in the right photonic processor.

We can then repeat the same kind of backward and forward process with these second (pink) lines of MZIs and their associated waveguides I_2 and O_2. This process will converge these second lines to find and implement the second most strongly coupled communications mode. If we had more diagonal lines in the processors, we could continue this process to establish successive communication modes.

The forward-and-backward algorithm described above was used to configure the two-processor system in the experiments shown in Figs. 1 and 2. While performing these experiments we realized that actually a forward-only propagation algorithm worked as well providing convergence of the system to the same final state. In the forward-only algorithm, the light is shown only in one direction and all the MZIs of the same line of the left and right processors are set at the same time. For instance, to establish the first communication mode, the light is injected from input I_1 and the 32 phase shifters of the first (blue) diagonal lines of MZIs are simultaneously driven to maximize the power at the output port O_1. Once the first communication channel is optimized, the procedure is repeated for the second channel (second pink diagonal lines of MZI). The main advantage of the forward-only algorithm is that it requires neither light sources at the receiver side, nor multiple iterations, so it makes the configuration more practical without affecting the degree of mode orthogonality with respect to the forward-and-backward algorithm (at least in all the examples considered in this work). Results reported in Fig. 3 and Extended Data Fig. 3 were obtained with the forward-only algorithm.

Control electronics. The control strategy employed for the automated self-configuration of the photonic processors is based on the implementation of local feedback loops that monitor and stabilize individually each MZI tuneable coupler [15]. To this end, dithering signals are applied to the thermo-optic phase shifters to identify the deviation from the optimum bias point [38] and maximize the optical power detected at an external photodetector (PD) coupled at the output port of the photonic chips. The external PD used in our experiment offers better sensitivity (about -55 dBm) than the standard integrated PDs available from the silicon foundry (about -35 dBm). Such an external PD allows to detect weaker light signals, as required when the automated configuration of the system starts from arbitrary conditions of the two processors and the coupling loss can be as high as 70 dB (see Supplementary Sec. 3). High-sensitivity integrated PDs would be more suitable for real applications and could provide an interesting solution for future implementations [39]. The electronic controller of the two-chip photonic system (counting 30 MZIs and 60 thermal phase shifters) is made of 4 customized motherboards, hosting each 16 parallel lock-in chains with phase shifter drivers and readout stages for the extraction of the error signal [Supplementary Fig. 2a]. Different pairs of orthogonal frequencies, ranging from 6.1 kHz to 47.6 kHz, are employed for the two phase shifters of each MZI. The electrical bandwidth of the feedback loop controller is limited by the frequency spacing between the dithering frequencies, thus resulting in a stabilization time of about 50 ms for each MZI line. The digital control electronics operate with 12 bits, meaning an accuracy of about 1mV as the control voltage on the thermal tuners is in the worst condition (5V). This corresponds to a phase uncertainty of the phase shift induced by the thermal tuners of about 1 mrad, which, in an ideal MZI, would lead to a negligible cross-talk of about -60 dB per MZI. For more details on the control electronics see Supplementary Sec. 2.

Photonic processor design and main building blocks. The integrated photonic processors are fabricated on a standard 220-nm Silicon Photonics platform (AMF foundry) and are designed for operation in the 1550 nm wavelength range. The photonic chip size is 5.8 mm $\times$ 1.3 mm. Supplementary Fig. 4 summarizes the main characteristics of the photonic building blocks used in the photonic processors. All the waveguides are single-mode channel waveguides with 500 nm width and a propagation loss of about 1 dB/cm. The on-chip array of apertures is implemented by means of a square 3×3 array of surface grating couplers (GCs) that couple the light into/from free space (Fig. 1c). The nine GCs of the 2D array are standard building blocks of the silicon photonics platform; no specific optimization of the GC design was carried out because the applications presented in this work apply to any kind of optical apertures. The center-to-center spacing of the GCs is $50\,\mu m \approx 32\lambda$, such spacing being constrained by the size of each GC (29.2 μm $\times$ 19.3 μm) and by the waveguide bundle required for routing the light from each GC to the input ports of the MZI processor. The periodicity in the far-field pattern (diffraction orders) is a consequence of the large spacing ($\gg \frac{\lambda}{2}$) between the array elements, which leads to multiple diffraction "replicas" of the underlying mode shapes. Such spacing is not a critical issue, because the presented results apply to any arbitrary spacing between apertures and also to randomly positioned apertures (non-periodic grid). For specific applications where grating lobes need to be mitigated, GCs with a smaller footprint can be designed in order to reduce the mutual spacing [40] and double-layer photonic platforms, such as silicon nitride on silicon [41], can be used to enable a more packed routing of the output waveguide array.

Each GC emits/receives TE polarized light within a radiation angle of $5^\circ \times 9^\circ$ centered around a 12° tilted direction with respect to the normal to the chip surface. The 2D array has an overall beamwidth of $0.6^\circ \times 0.6^\circ$, which is a field-of-view of about 1.7°. To observe experimentally the far field emitted by the two photonic chips, a 4f lens system is used, so that the plane of the apertures is Fourier transformed and collimated at a resulting Fourier plane between the two lenses, i.e., the far-field plane in Fig. 1b. Far-field measurements are performed with an IR camera that images this Fourier plane (see Supplementary Sec. 3 for more details on the experimental setup).

The MZIs have 3 dB directional couplers with 300 nm gap spacing between the coupled waveguides and 40 μm length of the coupling region. Phase shifters are realized through TiN thermal tuners (80 μm $\times$ 2 μm) deposited on top of the oxide above the waveguide, at a distance 2 μm above the silicon waveguide core. The thermal tuners have a power efficiency of 22 mW/π and a time response of about 10 μs. To mitigate thermal cross-talk issues, a thermal cross-talk cancellation technique [42] is used to improve the efficiency of the control algorithm. The power consumption for the full configuration of the two-processor system, including 30 phase shifters per chip, is about 1.3 W in the worst case where 2π phase shift would have to be applied to all the thermal tuners of the processor. Scalability of the system to larger scale circuits would benefit from the use of non-thermal actuators, exploiting materials with high electro-optic coefficients such as lithium niobate or barium titanate integrated in silicon waveguides, or opto-micromechanical phase shifters.

Loss analysis and wavelength dependence. Here we analyze the optical power budget for the free-space setup used in our experiments. The mesh processors do not introduce any fundamental loss for splitting or combining the beams, since they ideally implement unitary linear transformations. An overall on-chip loss of about 2 dB is observed, which is due to the propagation loss of the waveguides ($<$ 1 dB), bending loss, and the excess loss of the directional couplers ($<$ 0.05 dB each) of the MZIs. The coupling loss between the grating couplers and the in/out single-mode fibers is 4.5 dB per optical I/O. A 50:50 beam splitter (3 dB loss) is added in the free space optics for monitoring of the beam shapes with the near-IR camera at the far-field plane and an additional 3 dB loss is due to the aberration of the optical system and possible minor alignment tolerances in the experimental setup (see Supplementary Sec. 3). For the first-order mode, the end-to-end loss of the entire system in the absence of obstacles is about 35 dB, meaning that the coupling loss between the free-space mode and the 2D arrays is about 8 dB/array. Such loss can be substantially reduced by improving the fill factor of the 2D array or by using off-chip focusing/collimating optics, such as lenslet arrays in front of the grating couplers and/or telescopes; nonetheless, since SVD applies to generic non-unitary matrices, orthogonality of the established modes is always preserved even in highly lossy systems and through strongly diffractive/scattering media.

The GCs are connected to the photonic processor through optical waveguides with the same optical length in order to minimize the wavelength dependence of the entire circuit [29]. The wavelength range across which the photonic processors can operate is about 35 nm (from 1535 nm to 1570 nm) [29], this wavelength range is mainly limited by the wavelength-selective response of the GCs and by the wavelength dependence of the 3-dB directional couplers of the MZIs. Such wavelength dependence can be reduced by using optimized designs for broadband GCs [43] and for broadband directional couplers [44].

Scalability to larger optical systems. The effective number of available modes is associated with the non-zero singular values of the coupling matrix - that is, with the rank of $\mathbf{M_c}$ [12] - which is at most $\min(M, N)$. Each additional aperture (on both processors) can potentially increase the number of available channels. In the system with 3×3 apertures, up to 9 orthogonal modes exist, whose singular values are shown in Extended Data Fig. 2 (here we see that by reducing the number of gratings, the available number of modes decreases accordingly). Among them, the number of modes that can be found by the two-processor system is $\min(\hat{M}, \hat{N})$. The number of required MZI lines, $\hat{M}$ and $\hat{N}$, scales linearly with the number of modes to be found. Therefore, a system with 9×9 apertures (on both input/output sides $M = N = 81$) would need up to $M - 1 = 80$ MZI lines per processor to find all the modes, corresponding to $M(M-1)/2 = 3240$ MZIs.

By increasing the number of optical apertures, while keeping the same pitch, the coupling strengths (i.e. the singular values) of all the modes increase, as shown in Extended Data Fig. 2. This result is in line with the theory of phased array antenna systems, where by increasing the number of elements, the gain of the radiation pattern increases and the beam divergence reduces.

The extension of the approach to the case of chips that do not remain fixed in space does not lead to an increase in the complexity of either the photonic circuits or the configuration algorithm. In fact, each MZI of the transmitter (receiver) integrates an output (input) thermal tuner (see Supplementary Fig. 2) that is used to adjust the relative phase of the optical fields in the waveguide array. These phase shifters can be also used to provide the additional phase tilt that is required for scanning the beam, as happens in a LiDAR system [45]. As a result, pairs of orthogonal beams can be always found whatever the direction of arrival is, because any coupling matrix $\mathbf{M_c}$ can be decomposed according to SVD, and the two-processors system self-configures in the same way as in the case of fixed chips, regardless of the direction of the beams.

Data availability

All the data supporting the findings of this study are available within this Article and its Supplementary Information. Any additional information can be obtained from the corresponding authors on reasonable request.

Code availability

The computer codes that support the plots within this paper and other findings of this study are available from the corresponding author upon reasonable request.

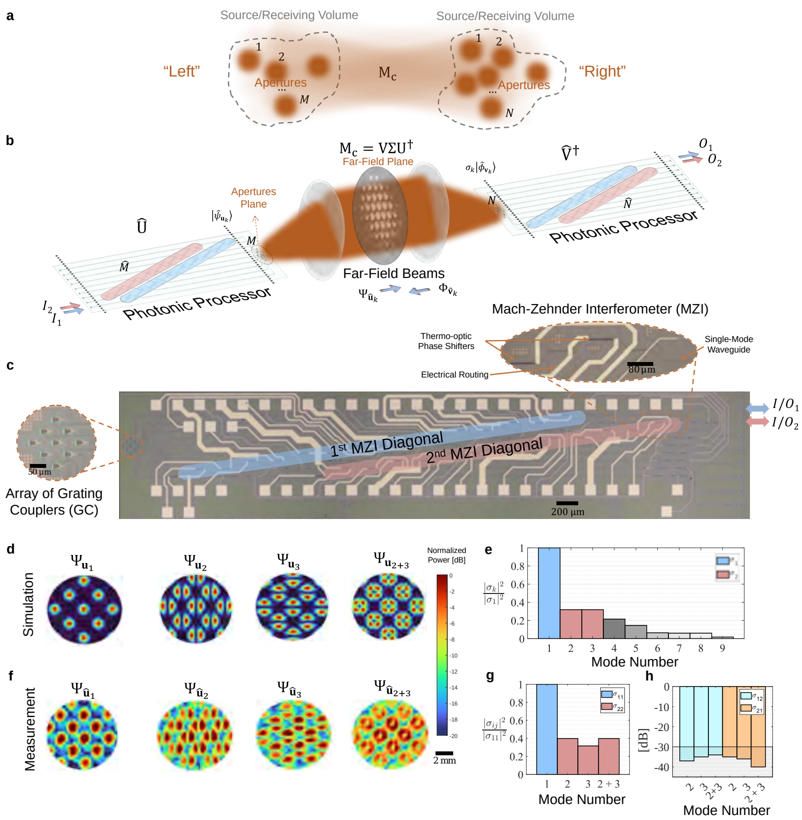

Fig. 1 Finding best orthogonal communication modes automatically with a pair of photonic integrated processors. a, Schematic of a generic optical system with M input and N output optical apertures in source and receiving volumes, respectively, which can be defined by a coupling matrix $\mathbf{M_c}$. **b**, Two programmable photonic integrated processors made of tuneable beam splitters connected to M (left-hand side) and N (right-hand side) optical apertures are used to automatically find pairs of orthogonal communication modes through arbitrary optical media. $I_{1,2}$ and $O_{1,2}$ are the input and output ports of the processor, respectively, which define end-to-end power coupling and cross-talk between two established channels. **c**, Top-view micro-photograph of the silicon photonic chip hosting 9 optical apertures (3×3 square array of grating couplers) connected to a two-diagonal mesh of thermally-tuneable MZIs. **d**, **f**, Far-field shapes of the first 3 modes that provide the highest coupling strengths between two symmetric sets of apertures ($M = N = 9$), as obtained in **d** numerically by computing the SVD of the system ($\Psi_{\mathbf{u}_k}$, $k = \{1, 2, 3\}$), and in **f** experimentally by finding them using a two-processor system ($\Psi_{\hat{\mathbf{u}}_k}$, $k = \{1, 2, 3\}$). Panels **e** (simulation, all 9 modes) and **g** (experiment, first 2 modes) show the coupling strengths (σ_{ij}, $i = j$) normalized to the first mode. Orthogonality between the different communication modes (σ_{ij}, $i \neq j$) is experimentally demonstrated by the low cross coupling (< -30 dB) in panel **h**. The error bar in the bar charts is about $\pm$ 1 dB for the optical cross-talk and less than 0.1 dB (about 2%) for the coupling strength.

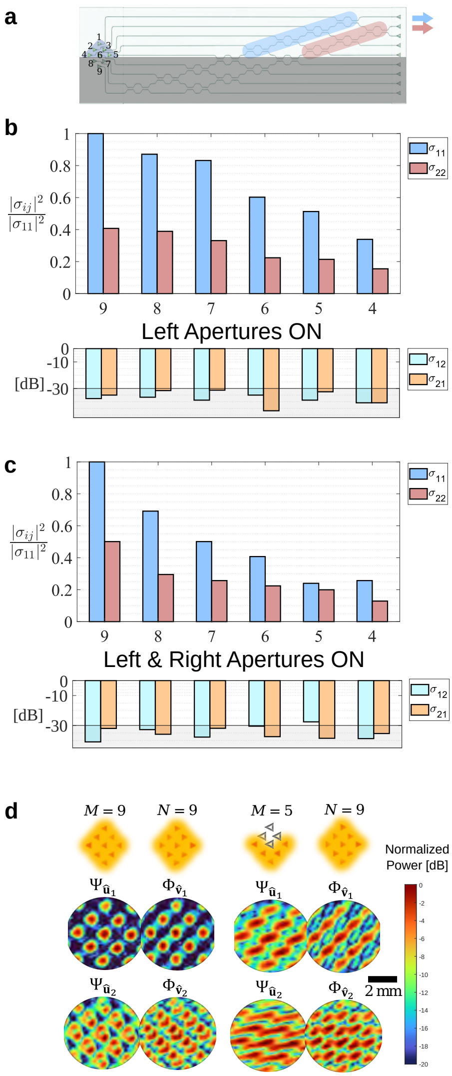

Fig. 2 Orthogonal modes between arbitrary sets of optical apertures. a, The number of input M / output N optical apertures in the source/receiving volume can be modified by controlling the corresponding MZIs of the mesh processors. Panels **b** and **c** show the measured input/output coupling strengths σ_{11} and σ_{22} of the first two modes (normalized to that of the first mode when $M = N = 9$) when the number of apertures is reduced according to a non-symmetric (panel **b**, $M = 9, 8, ..., 4;\ N = 9$) or (point-)symmetric configuration (panel **c**, $M = N = 9, 8, ..., 4$). A high degree of orthogonality between the first two modes (cross-talk < -30 dB, as shown by σ_{12} and σ_{21} bars) is experimentally achieved in both cases [see Extended Data Fig. 2 for comparison with simulations]. Selected far-field beam shapes of the left and right modes are shown in **d** for a symmetric case ($M = N = 9$) and a non-symmetric case ($M = 5, N = 9$) [See Extended Data Fig. 1 for complete set of beam shapes]. Error bars as in Fig. 1.

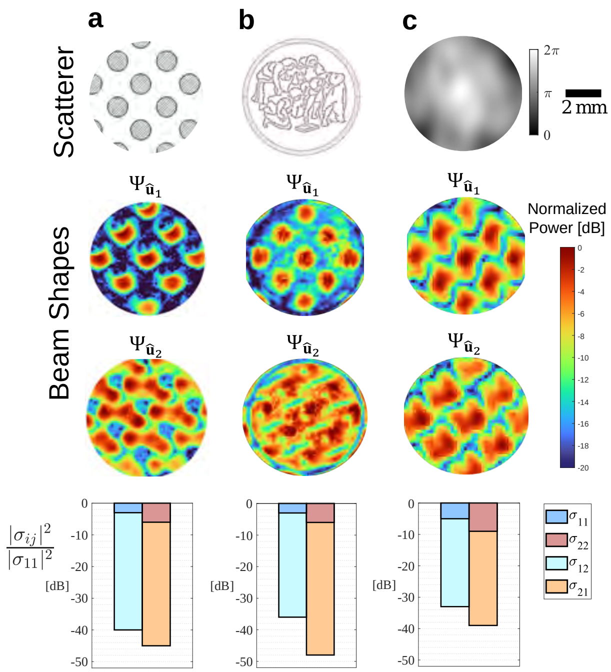

Fig. 3 Orthogonal modes through obstacles and scattering media. The two-processor system is used to find pairs of orthogonal optical beams propagating through different kinds of obstacles; **a**, periodic pattern of circular metal obstructions, **b**, micro-scale reproduction of the Politecnico di Milano logo, and **c**, phase-only aberrator. The far-field beam shapes providing maximum coupling strengths and minimum mutual cross-talk are shown. The four bars represent $\sigma_{ij}, i, j = \{1, 2\}$ normalized to the power of the first mode without obstacle in dB scale, all starting from zero. For those scatterers with a periodic pattern, the periodicity of the scatterers matches the periodicity of the diffraction orders of the beam in the scatterer plane. The peak-to-peak phase shift introduced by the phase-only aberrator is 2π. Error bars as in Fig. 1.

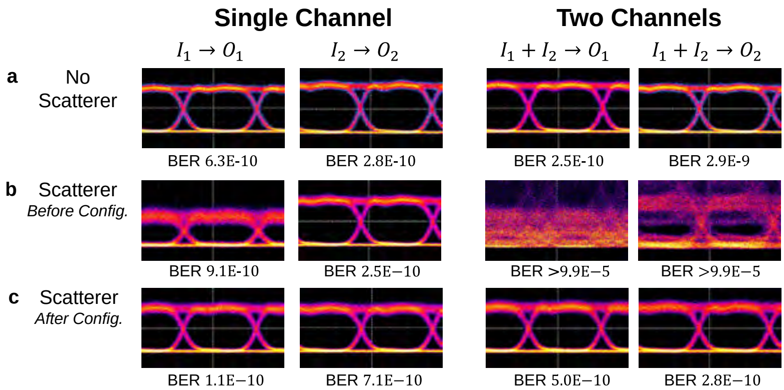

Fig. 4 Orthogonality between data communication channels. The performances of the two-processor system are assessed by transmitting two intensity-modulated NRZ-OOK signals at 5 Gbps. **a**, Eye diagrams and BER of the reference channels that are individually transmitted (only a single channel is switched on) through the system in the absence of any obstacle; when the interfering channel is switched on (two channels), no significant degradation is observed in the quality of the received signals. **b**, Insertion of an obstacle (specifically the donuts-like mask of Extended Fig. 3c is used here) breaks the orthogonality between the communication modes causing strong channel interference and signal degradation. **c**, The reconfiguration of the two-processor system enables the establishment of a new pair of orthogonal modes that can be transmitted through the obstacle with negligible mutual crosstalk.

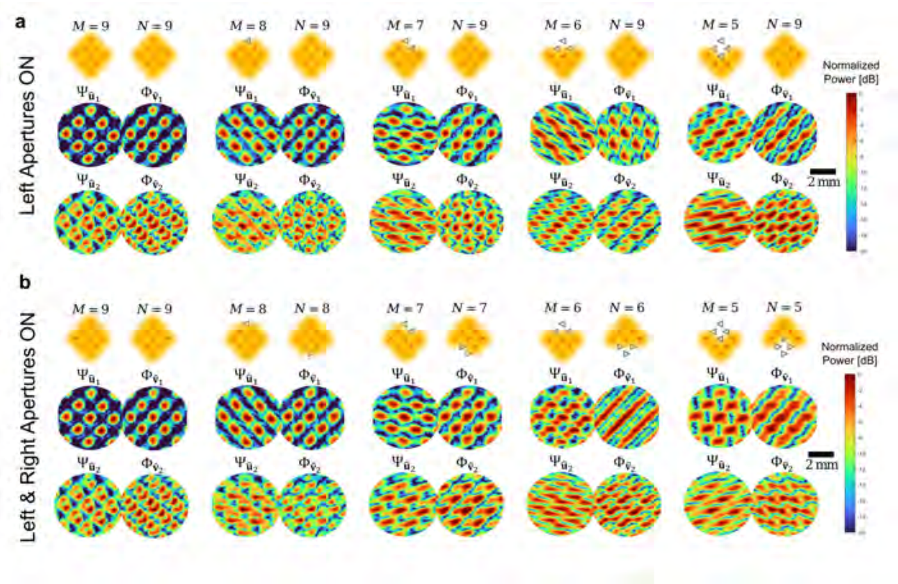

Extended Data Fig. 1 Beam shapes of orthogonal modes between arbitrary sets of optical apertures. Complete set of beam pairs (far fields $\Psi_{\hat{\mathbf{u}}_{1,2}}$ and $\Phi_{\hat{\mathbf{v}}_{1,2}}$) measured when the number of input M / output N apertures in the source/receiving volumes are progressively reduced, **a** in a non-symmetric configuration ($M = 9, 8, ..., 5$; $N = 9$), and **b** in a (point-)symmetric configuration ($M = N = 9, 8, ..., 5$).

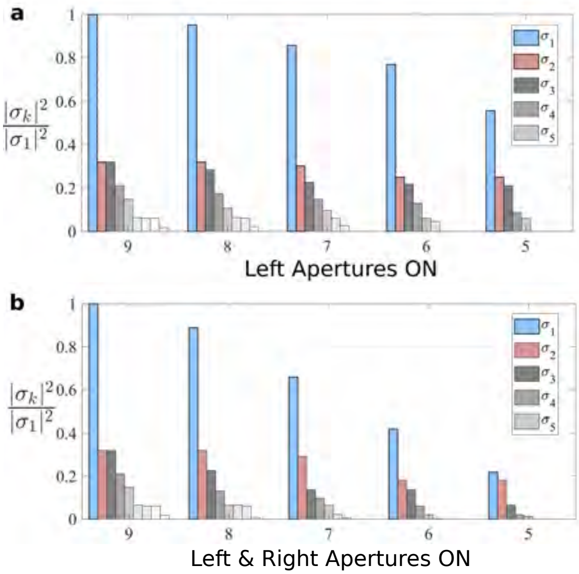

Extended Data Fig. 2 Coupling strength of mode pairs established between arbitrary sets of optical apertures. Simulated coupling strengths of modes established between the source/receiving volumes when the number of input M and output N apertures are progressively reduced **a** in a non-symmetric configuration ($M = 9, 8, ..., 5$; $N = 9$), and **b** in a (point-)symmetric configuration ($M = N = 9, 8, ..., 5$). Coupling strengths are normalized to that of the first mode when $M = N = 9$. Experimental data are shown in Fig. 2b,c, while measured beam shapes are reported in Extended Data Fig. 1.

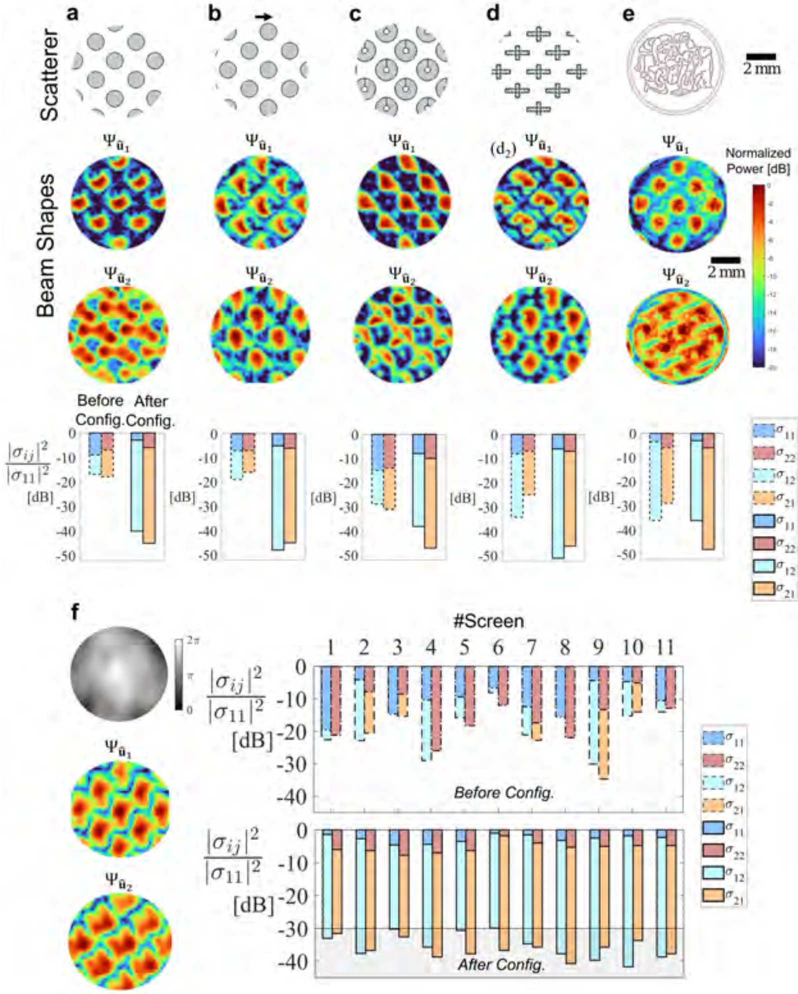

Extended Data Fig. 3 Orthogonal modes through obstacles and scattering media. The full set of obstacles used in the experiments include metal obstructions arranged as a periodic pattern of **a** circles (and laterally shifted in **b**), **c** donuts, **d** crosses, and **e** a microscale reproduction of the Politecnico di Milano logo. The far-field beam shapes of the first two modes $\Psi_{\hat{\mathbf{u}}_{1,2}}$ providing the maximum coupling strengths and the minimum mutual cross-talk through these obstacles are shown. For each case, bar charts show the coupling strength ($\sigma_{ij},\ i = j$) and the mutual cross-talk ($\sigma_{ij},\ i \neq j$), which are both deteriorated with the insertion of the obstacle (dashed bars, before configuration), and can be mostly recovered by optimizing the two photonic processors (solid bars, after configuration). In the experiments reported in panel **f** the obstacle is a phase aberrator emulated by using an SLM; the recovery of the coupling strength ($\sigma_{ij},\ i = j$) and the mutual cross-talk ($\sigma_{ij},\ i \neq j$) is shown for 11 different example configurations of the SLM. The peak-to-peak phase shift introduced by the phase-only aberrator is 2π.

Contents

1. Self-configuring algorithm

In this section, we present a detailed discussion of the self-configuration algorithm used for the automated control of the two-processor system. With respect to the description of the algorithm that is given in the Methods, here a formal mathematical treatment is reported, which demonstrates, with the support of numerical simulations, the convergence of the system to the implementation of the SVD of the coupling matrix $\mathbf{M_c}$. Part of this discussion can be also found in [1], where this system was theoretically conceptualized, but it is reported here for completeness.

The input light beam to the aperture array on the photonic processor is "sampled" by the apertures (grating couplers) and leads to corresponding complex optical amplitudes in the single-mode optical waveguides to which they are connected. Mathematically stated, we can consider an input vector $|\psi_{in}\rangle = [u_1 \dots u_M]^T$ with elements $u_j,\ j = \{1, \dots M\}$ given by the overlap integral between the field amplitude of the input beam impinging on the array and the near field of the j-th grating coupler of the array. This vector $|\psi_{in}\rangle$ is the input to a matrix $\hat{\mathbf{U}}_{[\hat{M}\times M]}$ that describes the photonic processor with $\hat{M}(\leq M)$ diagonal "rows", and the output complex vector $|\psi_{out}\rangle = [w_1 \dots w_{\hat{M}}]^T$ gives the resulting output optical amplitudes in the single-mode output waveguides (e.g., O_1 and O_2 in Fig. 1). Explicitly, we can write

$$|\psi_{out}\rangle = \hat{\mathbf{U}}|\psi_{in}\rangle \tag{1}$$

with

$$\hat{\mathbf{U}} = \begin{bmatrix} \langle\hat{\psi}_{\mathbf{u_1}}| \\ \langle\hat{\psi}_{\mathbf{u_2}}| \\ \vdots \\ \langle\hat{\psi}_{\mathbf{u}_{\hat{M}}}| \end{bmatrix} \tag{2}$$

where the rows of the matrix $\langle\hat{\psi}_{\mathbf{u}_i}|,\ i = \{1, \ldots, \hat{M}\}$ are controlled by the settings of the phase shifters within the MZIs, and in the case of a lossless device, they are orthonormal, being the unitary matrix $\hat{\mathbf{U}}$.

In operation as a self-configuring processor here, we presume first that we shine in some light beam that results in some vector $|\psi_{in_1}\rangle$ of complex amplitudes in the input waveguides. In using the processor, we proceed first by a "self-configuration" process to set the MZIs in the first diagonal row [see Supplementary Fig. 1a]. Explicitly, starting from the bottom MZI in the first diagonal row, we adjust the phase shifters in that MZI so that no power emerges from the lower "drop port" output. If the beamsplitters in the MZI are 50:50, such an adjustment is always possible for any specific pair of input amplitudes for that MZI, and it can be achieved by two successive power minimizations in that lower output, one achieved by adjusting the input phase shifter ϕ on the input waveguides, and the second by adjusting the internal phase shifter θ on one of the MZI internal arms; this results in a zero power at the bottom drop port. As a result of this first step, all the power in the lowest two input guides is now present on the upper output waveguide of the first MZI. We then similarly configure the next MZI in the row to minimize the power to zero in its bottom output, thus combining all the power from the lower three waveguides to the upper output of this MZI. We can then proceed similarly up the remaining MZIs in the diagonal line, with the result that all the power in M input waveguides now emerges from the top output waveguide, i.e., $w_i = \langle\hat{\psi}_{\mathbf{u}_i}|\psi_{in_1}\rangle = 0, i \neq 1$; this operation can be described as a "self-aligning beam coupler" [2]. Note that this explicitly means that for the input beam $|\psi_{in_1}\rangle = \alpha_1|\hat{\psi}_{\mathbf{u}_1}\rangle$ being $\alpha_1(= w_1)$ related to the power in the input beam $|\alpha_1|^2 = ||\psi_{in_1}||^2 = \langle\psi_{in_1}|\psi_{in_1}\rangle$ and $|\psi_{in_1}\rangle$ is orthogonal to all other rows of the $\hat{\mathbf{U}}$.

A second important behavior of this processor is what happens if, while holding these settings of the first diagonal row of MZIs, we shine a second beam into this device, specifically a second beam for which the vector of amplitudes $|\psi_{in_2}\rangle$ is orthogonal to the first beam $|\psi_{in_1}\rangle$ — that is, for which the product $\langle\psi_{in_2}|\psi_{in_1}\rangle = \langle\psi_{in_1}|\psi_{in_2}\rangle = 0$. In this case, to the extent that this processor can be treated as lossless, none of the power in this second input beam can appear in the "top" output waveguide, i.e., $w_1 = \langle\hat{\psi}_{\mathbf{u_1}}|\psi_{in_2}\rangle = 0$. Hence, all the power in the second beam $|\psi_{in_2}\rangle$ must appear in the "lower" outputs of the MZIs in the first row. However, those outputs are connected to a second row of MZIs, and we can now simply self-align this second row to give all the power in the second output waveguide on the right (i.e., $w_i = \langle\hat{\psi}_{\mathbf{u}_i}|\psi_{in_2}\rangle = 0, i \neq 2$) by minimizing (to zero) the powers in their outputs. In the case of more orthogonal inputs, the following implemented MZI rows can self-align in the same way to couple the power of these modes to different output waveguides (up to $\hat{M}$ modes). Therefore, as shown schematically in Supplementary Fig. 1, we can write

$$\begin{bmatrix} ||\psi_{in_1}|| & & & 0 \\ & ||\psi_{in_2}|| & & \\ & & \ddots & \\ 0 & & & ||\psi_{in_{\hat{M}}}|| \end{bmatrix} \mathbf{\Theta} = \hat{\mathbf{U}} \begin{bmatrix} \\ |\psi_{in_1}\rangle & |\psi_{in_2}\rangle & \dots & |\psi_{in_{\hat{M}}}\rangle \\ \\ \end{bmatrix} \tag{3}$$

with $||\psi_{in_i}||^2 = \langle\psi_{in_i}|\psi_{in_i}\rangle,\ i = \{1,\dots,\hat{M}\}$ being the power of i-th input mode which is coupled to corresponding i-th output waveguide, and $\mathbf{\Theta}$ a diagonal matrix consisting of arbitrary phase shifts $e^{\sqrt{-1}\theta_i}, i = \{1,\dots,\hat{M}\}$ on the diagonal.

Note that now if we run the processor backward, considering the reciprocity of the processor, we get:

$$\hat{\mathbf{U}}^T = (\hat{\mathbf{U}}^\dagger)^* = \begin{bmatrix} \\ \\ |\hat{\psi}_{\mathbf{u}_1}\rangle & |\hat{\psi}_{\mathbf{u}_2}\rangle & \ldots & |\hat{\psi}_{\mathbf{u}_{\hat{M}}}\rangle \\ \\ \\ \end{bmatrix}^* \tag{4}$$

which are the conjugated input fields $|\hat{\psi}_{\mathbf{u}_i}\rangle = (1/\alpha_i)\,|\psi_{in_i}\rangle,\ i = \{1, \ldots, \hat{M}\}$ that are embedded in the phase shifters of the processor.

It is, of course, possible to calculate all the settings of the phase shifters in the MZIs that will give the necessary elements in $\hat{\mathbf{U}}$, and the algebra for that is straightforward, but we never have to perform these calculations when we set this system up by self-configuration as we do here. The matrix $\hat{\mathbf{U}}$ is a consequence of the orthogonal vectors we chose to separate; it is set up effectively by this physical self-configuration process, and in the operation of the device we do not need to know explicitly what this matrix is, even though it gives a mathematical way to look at the resulting process.

In the implementation, we can make use of mostly-transparent photodetectors (PDs) at the various drop ports (either transparent PDs such as in [3] or integrated tap monitors). In this case, the PDs remain in place even as we minimize successive diagonal lines of MZIs. It is also possible to run the self-configuring algorithms based on maximizing the power at the outputs rather than minimizing power at the internal drop ports [4] [see Supplementary Fig. 1a]. This can have the advantage of using bench-top PDs with higher sensitivity, reducing the cost of chip fabrication, and required electronics for readout.

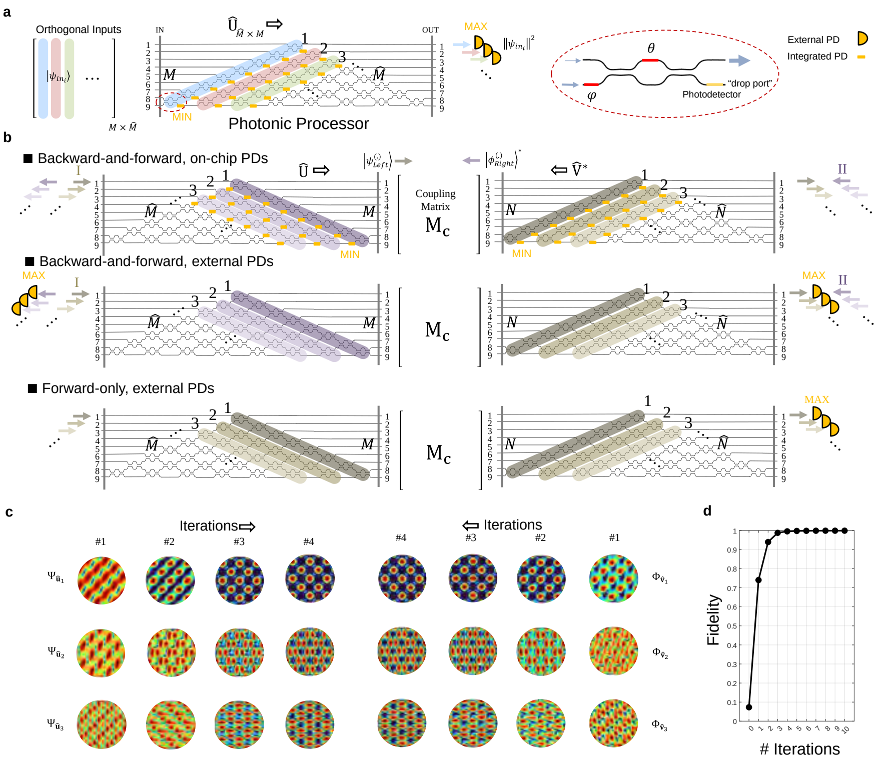

Fig. 1 Self-configuration of the two-processor system. **a**, Different orthogonal inputs $|\psi_{in_i}\rangle$ are shone to the inputs of the mesh and by configuring the different rows of MZIs (as shown with different colors), the power of the beams can be coupled to different output waveguides [panel **a**]. To his aim, either a minimization process on each MZI in a row or a maximization of the top output waveguide of the mesh can be done. A single MZI can be configured automatically in order to sum up coherently the two arbitrary inputs so that all the power appears in only one of the outputs (i.e., the upper output, while the lower output is the "drop" port). This can be done by adjusting two phase shifters ϕ and θ in the external and internal arm of the MZI, respectively. **b**, The two-processor apparatus can be used to "analyze" a coupling matrix $\mathbf{M_c}$. This can be done either by running both meshes backward and forward iteratively till reaching a stable solution, or by using a forward-only approach for maximizing MZI rows in both meshes at the same time. Panel **c** shows the evolution of the beams of the first 3 modes with the largest coupling strengths shone from left and right to converge to the solution. The convergence of this example case, starting with arbitrary settings of MZIs on both sides is shown in panel **d** in terms of *fidelity* between the actual $\mathbf{\Sigma}$ and estimated singular values $\hat{\mathbf{\Sigma}}$.

Similar self-configuring algorithms described above for a photonic processor can be performed in the two-processor apparatus presented in this work. Supplementary Fig. 1b shows schematically some of these approaches which are summarized here:

- A backward and forward (B&F) approach using power minimization in on-chip integrated PDs, as suggested in [1];
- same B&F approach, but using external PDs for each diagonal row of MZIs;
- a forward-only approach, in which corresponding diagonals of MZIs in the left-right mesh self-configure to only one external PD at one side.

To explain the algorithm in mathematical terms, we can consider a coupling matrix for the left and right apertures, decomposed as

$$\mathbf{M_c} = \mathbf{V\Sigma U}^{\dagger} = \sum_{k=1}^{r} |\phi_{\mathbf{v}_k}\rangle \sigma_k \langle \psi_{\mathbf{u}_k}| \tag{5}$$

with $r = \operatorname{rank} \mathbf{M_c}$ (Eq. 2 in the main text, Methods section). Then, we consider the two processors connected to the left and right apertures as being represented by two unitary matrices $\hat{\mathbf{U}}$ and $\hat{\mathbf{V}}$ (here as operator from "output" waveguides to apertures), respectively, as in Supplementary Fig. 1b. Now if we inject the light to the first input waveguide of the left processor, since, initially, the phase shifts on the MZIs are arbitrary, we will get a complex amplitude field $|\psi^{(0)}_{Left}\rangle$ coming out of the processor just before the left aperture, which we can expand in the complete basis set $\{|\psi_{\mathbf{u}_m}\rangle\}_{m=1}^{M}$ as

$$\begin{aligned} |\psi^{(0)}_{Left}\rangle &= \left(\sum_{m=1}^{M} |\psi_{\mathbf{u}_m}\rangle\langle\psi_{\mathbf{u}_m}| \right) |\psi^{(0)}_{Left}\rangle \\ &= \alpha_L^{(0)} \sum_{m=1}^{M} \lambda_m |\psi_{\mathbf{u}_m}\rangle \end{aligned} \tag{6}$$

with $\alpha_L^{(0)}\lambda_m = \langle\psi_{\mathbf{u}_m}|\psi^{(0)}_{Left}\rangle$ where $\alpha_L^{(0)}$ is a factor related to the power of the beam $|\alpha_L^{(0)}|^2 = ||\psi^{(0)}_{Left}||^2$. If we propagate this field from left to right, after coupling to the right apertures we get

$$\begin{aligned} |\phi^{(0)}_{Right}\rangle &= \mathbf{M_c}|\psi^{(0)}_{Left}\rangle \\ &= \left(\sum_{k=1}^{r} |\phi_{\mathbf{v}_k}\rangle \sigma_k \langle \psi_{\mathbf{u}_k}|\right) |\psi^{(0)}_{Left}\rangle \\ &= \alpha^{(0)}_{L} \sum_{k=1}^{r} \sigma_k \lambda_k |\phi_{\mathbf{v}_k}\rangle. \end{aligned} \tag{7}$$

Then, we configure the first MZI row $\langle\hat{\phi}_{\mathbf{v}_1}|$ on the right processor $\hat{\mathbf{V}}$ to couple the mode power to the output waveguide, i.e., $|\langle\hat{\phi}_{\mathbf{v}_1}|\phi^{(0)}_{Right}\rangle|^2 = ||\phi^{(0)}_{Right}||^2$. After configuration of the first row, we inject the light back to the first "input" waveguide of the right processor, and as discussed before, we get a complex-amplitude field proportional to $|\hat{\phi}_{\mathbf{v}_1}\rangle^*$ and thus $|\phi^{(0)}_{Right}\rangle^*$ which can be written as

$$|\phi^{(1)}_{Right}\rangle^* = \alpha^{(1)}_{R} \sum_{k=1}^{r} \left(\sigma_k \lambda_k |\phi_{\mathbf{v}_k}\rangle\right)^* \tag{8}$$

with $\alpha^{(1)}_{R}$ a factor related to the injected power. This field passes backward again through the medium (which is presumed to be reciprocal), and hence we can write the backward coupling matrix as

$$\mathbf{M}_c^T = (\mathbf{M}_c^\dagger)^* = \sum_{k=1}^{r} (|\psi_{\mathbf{u}_k}\rangle \sigma_k^* \langle \phi_{\mathbf{v}_k}|)^* \tag{9}$$

so what we get again after coupling to the left apertures can be written as follows

$$\begin{aligned} |\psi^{(1)}_{Left}\rangle^* &= \mathbf{M}_c^T |\phi^{(1)}_{Right}\rangle^* \\ &= \alpha^{(1)}_R \sum_{k=1}^{r} |\sigma_k|^2 \lambda_k^* |\psi_{\mathbf{u}_k}\rangle^* \end{aligned} \tag{10}$$

for which we then perform the self-configuration of the first MZI row $\langle\hat{\psi}_{\mathbf{u}_1}|$ on the left processor and couple the mode power. Therefore, starting this loop again, we can write the initial (conjugated) field propagating from left to right as

$$|\psi^{(2)}_{Left}\rangle = \alpha^{(2)}_L \sum_{k=1}^{r} |\sigma_k|^2 \lambda_k |\psi_{\mathbf{u}_k}\rangle \tag{11}$$

and after another round trip, we get

$$|\psi^{(4)}_{Left}\rangle = \alpha^{(4)}_L \sum_{k=1}^{r} |\sigma_k|^4 \lambda_k |\psi_{\mathbf{u}_k}\rangle \tag{12}$$

and so on. Considering the fact that $1 \geq \frac{|\sigma_2|}{|\sigma_1|} \ldots \geq \frac{|\sigma_r|}{|\sigma_1|}$, we can write then for the p-th round-trip (p even)

$$|\psi^{(p)}_{Left}\rangle = \alpha^{(p)}_L \left[|\sigma_1|^p \sum_{k=1}^{r} |\frac{\sigma_k}{\sigma_1}|^p \lambda_k |\psi_{\mathbf{u}_k}\rangle \right]. \tag{13}$$

We can see that if we go sufficiently enough through this loop

$$\Rightarrow |\psi^{(p)}_{Left}\rangle \xrightarrow{p\rightarrow\infty} \alpha^{(p)}_L |\sigma_1|^p \lambda_1 |\psi_{\mathbf{u}_1}\rangle = \alpha|\psi_{\mathbf{u}_1}\rangle \tag{14}$$

and also $|\phi^{(p)}_{Right}\rangle \xrightarrow{p\to\infty} \beta|\phi_{\mathbf{v}_1}\rangle$. The same procedure holds for the configuration of the following MZI rows, and thus we can conclude that the MZI mesh processors on the left $\hat{\mathbf{U}}$ and right $\hat{\mathbf{V}}$ are effectively implementing the left and right singular vectors of the coupling matrix $\mathbf{M_c}$, i.e., $\mathbf{U}$ and $\mathbf{V}$, respectively.

In principle for a given coupling matrix $\mathbf{M}_c$ different forms of SVD solutions exist, which are associated with different permutations of the singular values along the diagonal matrix $\mathbf{\Sigma}$ and a different phase term in the singular values. Among these solutions, the two-processor system configured by the power maximization algorithm finds the one where the singular values are sorted in decreasing order.

Supplementary Fig. 1c shows a simulated example of the two-processor self-configuration procedure which is implemented for the case of Fig. 1 of the main text. Panels show examples of the far-field beam shapes of the first 3 modes shone from left $\Psi_{\hat{\mathbf{u}}_k}$ and right $\Phi_{\hat{\mathbf{v}}_k}$, $k = \{1, 2, 3\}$, respectively, starting from initial random settings of the MZIs on both sides. As can be seen, after a number of iterations, the beam shapes evolve into the shapes of the eigenmode pairs as considered in 1d of the main text. A figure of merit that we can consider here is the so-called *Fidelity* between the actual solution $\mathbf{\Sigma}$ (singular values) and the estimated one $\hat{\mathbf{\Sigma}} = \hat{\mathbf{V}}^\dagger \mathbf{M_c} \hat{\mathbf{U}}$, defined as

$$F(\hat{\mathbf{\Sigma}}, \mathbf{\Sigma}) = \left| \frac{tr(\hat{\mathbf{\Sigma}}^\dagger \mathbf{\Sigma})}{\sqrt{tr(\hat{\mathbf{\Sigma}}^\dagger \hat{\mathbf{\Sigma}}) tr(\mathbf{\Sigma}^\dagger \mathbf{\Sigma})}} \right|^2$$

with $tr(.)$ being the trace of the matrix. Supplementary Fig. 1d shows the evolution of this figure for a number of iterations which eventually converges to 1, confirming the fact that $\hat{\mathbf{\Sigma}} \to \mathbf{\Sigma}$.

2. Control electronics

The feedback strategy to control the MZI mesh is based on the dithering technique, which allows tuning and locking the working point of each MZI without prior calibrations of the system [5]. Supplementary Fig. 2a shows the working principle of the technique applied to a single MZI. There are two phase shifters or actuators in each such MZI. For each such phase shifter, we add a small sinusoidal oscillation voltage - a "dithering" - on top of the DC bias voltage, making the device transfer function vibrate around its bias point with an oscillation depth proportional to the transfer function's first derivative. We choose such dithering signals at different frequencies for the two different phase actuators. The effect of each phase actuator can be discriminated by means of a lock-in technique used to identify each such frequency component by properly demodulating and low-pass filtering the electrical output signal from the PD. In this way, the MZI transfer function and its partial derivatives with respect to the applied phase shifts can be extracted in real-time (different panels in Supplemetary Fig. 2a). In the reported experiments, a dithering voltage of 50 mV was chosen to avoid relevant impacts on the intensity level of the optical beam at the output of the system.

The information on the partial derivatives is then exploited to control the MZI working point. In our experiments this working point is set to a stationary point (minimum/maximum) of its transfer function by a simple feedback loop acting on the DC bias voltage, nulling out the detected dithering signal. Compared to other techniques for setting MZIs, this approach does not require any prior calibration, since the condition of null output dithering oscillation only depends on the MZI transfer function and not on any other parameters of the system, such as input light power or temperature. The voltage driving each phase shifter is automatically set by two parallel integral controllers, each fed with one of the two partial derivative signals [Supplementary Fig. 2b]. The set-point of the loop is the amplitude of the target derivative signal (which is zero in this case). By tuning the gain k of the controller, the bandwidth of the control loop can be set to achieve the desired update speed and accuracy. By inverting the signal at the input of the controller it is possible to target both minima and maxima of the MZI transfer function, effectively steering all the light to the upper or lower output port of the device.

The dithering technique can be effectively used to automatically control all of the MZIs in a given diagonal row of the photonic processors. To this end, if a PD is integrated at the lower output port of each MZI [such as in Supplementary Fig. 2c], independent control loops can be implemented for each MZI and the same dithering frequencies can be reused. In this case, the configuration of the MZI row proceeds in a forward direction starting from the first MZI and progressively proceeding to the last one in the row until all the light is steered to the upper output port.

In the photonic processors used in this work, there are no integrated PDs and a different control approach is used, instead, as shown in Supplementary Fig. 2d. A single external PD is coupled at the upper output port of the circuit (where the light intensity has to be maximized) to control all the MZIs simultaneously. In order to discriminate the effect of each individual phase shifter on the optical output of the MZI processor, each actuator needs to be labeled with a different dithering frequency. With this approach, the control system implements a nested multivariable gradient descent algorithm, starting from the last MZI and proceeding backward to maximize the light intensity at the output until all the MZIs are correctly tuned.

Both control approaches allow us to automatically compensate in real-time for any drift in the mesh working condition by keeping the feedback loops active. The use of an integrated PD for each MZI is advantageous since it allows us to split the tuning procedure into independent local feedback loops and it requires only two orthogonal dithering signals, thus simplifying the lock-in detection and enabling a faster configuration time. Indeed, since the maximum tuning bandwidth is limited by the frequency difference of the dithering signals, by using only two tones it is possible to space them sufficiently apart to achieve a higher configuration speed. However, such an approach has a significant overhead in terms of electronic complexity, since each PD requires a specific readout circuit. In addition, for photonic processors with more than one MZI diagonal, transparent PDs are needed [3], which typically have lower sensitivity than conventional PDs.

In our experiments, the use of a single output PD allows using only one readout chain for a complete MZI diagonal, thus simplifying the acquisition electronics. In addition, the external PD that we used (see Supplementary Sec. 3) offers better sensitivity than integrated ones, enabling us to discriminate weaker light signals. On the other hand, the nested control approach and the use of multiple dithering frequencies limits the bandwidth of the closed-loop control system, which in our experiments is about 50 ms for each MZI row. Such time response is limited by the filter that is used to select the dithering frequencies applied to the phase shifters of each MZI, which in our experiments are between 6.1 kHz to 47.6 kHz. The response time can be improved by using faster integrated phase shifters, more sensitive photodetectors, and more spaced dithering frequencies (or independent local feedback loops by means of integrated PDs).

As described in the Methods, the setting of multiple modes is enabled by shining in one mode at a time and by sequentially lining up subsequent diagonal rows of the processors. Before being coupled to the first processors, the optical beams can be conveniently labelled with a shallow amplitude modulation (pilot tone) in such a way that the contribution of each mode can be discriminated by the PD coupled at the output ports of the second processors [4, 6]. Frequency domain plots are shown in Supplementary Fig. 2e for both control strategies discussed in this section. Each dithering frequency now has side-band signals, corresponding to the labeled modes. The mesh configuration is thus performed in the same way described as before, but instead of detecting tones at f_{dx}, the readout is performed at $f_{dx} \pm f_{tone,1}$ for the first diagonal of the processor and $f_{dx} \pm f_{tone,2}$ for the second one. In this way, it is possible to maintain the control feedback always active during the operation of the processors without switching the transmitted signals on and off. Mode labeling with pilot tones enables an adaptive control of the photonic processors to maintain the optimum orthogonal channels through time-varying systems, such as turbulent media.

All these strategies have been embedded into a custom electronic system developed to control the two photonic processors. The platform has a modular structure, made of two printed circuit boards (PCB). An interface board hosts the photonic chip (Supplementary Fig. 2f), with a suitable shape to best fit on the optical setup (see Supplementary Sec. 3). Each chip is wire-bonded to the board to provide all the electrical signals needed for operation. A main control motherboard, connected with cables to the interface PCB, houses all the electronics needed to bias the on-chip sensors, acquire their output signals and drive the actuators (Supplementary Fig. 2g). The board can also connect to external bench-top instruments, to control the photonic processors with a single external power monitor. An FPGA on the motherboard performs the lock-in detection and implements in the digital domain the feedback laws described in this section. A custom graphical user interface allows one to set

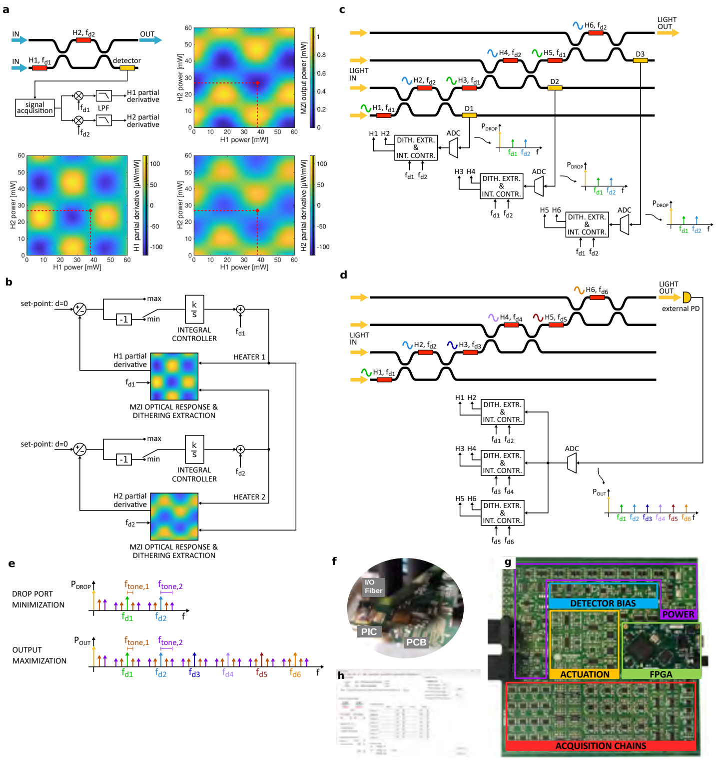

Fig. 2 Closed-loop control of a photonic processor. The control scheme for a single MZI, shown in **a**, is based on the dithering technique, which allows extracting the device transfer function in real-time (MZI output power map), as well as its partial derivatives with respect to the two thermal tuners power (H1 and H2 partial derivatives). The two partial derivatives are then fed to integral controllers, shown in **b**, to automatically tune the working point of each MZI to maximize/minimize the light at their output. **c**, The approach can be straightforwardly applied to a MZI processor when each device is monitored with an integrated PD, however, as shown in **d**, it can also be adapted to control the whole circuit with a single external PD at the output. **e**, Pilot tones can be used to label each optical mode that is injected in the system and discriminate its effect in the readout of the PDs, thus allowing to employ the same control strategy even when multiple beams are simultaneously shone. The configuration of the photonic processors is performed by a custom electronic system, made of an interface board placed on the optical bench (panel **f**), connected to a motherboard containing the readout and actuation circuits (panel **g**). A graphical user interface (panel **h**) allows one to monitor the state of the system with a personal computer.

up the electronic system and visualize in real-time the configuration state of the photonic processors, as shown in Supplementary Fig. 2h).

3. Experimental setup

The experimental setup employed in the experiments presented in this work is shown in Supplementary Fig. 3(a).

The free-space optics between the two photonic integrated processors includes two biconvex (best form) lenses with a focal length $f = +50$ mm that are positioned in a $4f$ configuration. Two turning mirrors are positioned on top of the photonic chips to steer the optical beam radiated by the grating couplers to the horizontal direction, which emits at an angle of 12° with respect to the normal to the chip surface.

Considering the forward propagation of the light from left to right (actually the same happens also in the backward direction), the optical field at the plane of the grating coupler array of the left processor is Fourier transformed at the back focal plane of the first lens [plane P in Supplementary Fig. 3a]. The optical field is then transformed again by the second lens and focused on the grating couplers plane (image plane) of the 2nd processor. A near-IR camera (Xenics Bobcat 640) is focused on the far-field plane to capture the shape of the beams that are radiated by the left and the right processor. To this end, a 50:50 beam splitter (BS_1) is positioned in the Fourier plane of the system. In the experiments shown in Fig. 3 and in the Extended Data Fig. 3 of the main text, the amplitude mask (obstacle) is inserted close to the beam splitter. In the experiment with the spatial light modulator (SLM), the camera is replaced by the SLM, and an additional 90:10 splitter (BS_2) is added before/after the SLM to monitor the light beam shape using the camera (this setup configuration is shown in the picture of Supplementary Fig. 3c and d).

Single-mode (SM) fibers are positioned on top of the in/output grating couplers of the left/right photonic processors using two 3-axis micro-positioners. The input fiber of the system is coupled to a 1550 nm laser source (ANDO

AQ4320D), which is amplified by an erbium-doped fiber amplifier (EDFA, IPG Photonics EAD-1K-C) up to a power level of +15 dBm before being coupled to the input waveguide port of the left photonic processor. Such an EDFA is used to compensate for the very high loss of the system before optimization, which can be as high as 70 dB. By launching an input power of +15 dBm at the ports I_1 and I_2 of the transmitting chip, an output power of at least -55 dBm is available at ports O_1 and O_2 at the output, which is above the sensitivity of the external PD. The ASE noise of the EDFA, which spans across a wavelength range of more than 40 nm, is responsible for some reduction of the optical cross-talk between the orthogonal modes because such a large noise spectrum is larger than the operational bandwidth of the processor. By cascading an ASE rejection filter centered around the carrier wavelength of the considered channels (1550 nm) a higher rejection can be achieved.
A fiber polarization controller is used to align the polarization state of the light at the input of the left processor to the transverse electric (TE) mode of the grating coupler.

At the output port of the right processor, a fiber splitter is used to tap 90% of the optical power towards the monitor PD (Newport 1811) used by the electronic control system (see Supplementary Sec. 2), and 10% to a power meter (HP 81521B) used for the measurement of the communication modes power (i.e. coupling strength $\sigma_{ij}, i = j$ and cross-talk $\sigma_{ij}, i \neq j$). The four customized electronic motherboards described in Supplementary Sec. 2 are connected to the PCBs hosting the photonic chips. In the forward and backward algorithm, the input and output fibers are iteratively swapped in order to reverse the direction of the light propagation (this procedure is operated by swapping the connection of the input/output patch cords between the source and PD side of the setup). In the forward-only algorithm, the monitor PD is used to provide the feedback signal to all four motherboards controlling the two photonic processors. The temperature of both chips is stabilized using thermo-electric coolers (TEC), placed underneath the PCBs.

In the experiments carried out in this work, when the two photonic processors are not optimized for maximum end-to-end coupling through a given optical medium (for instance if the thermal phase shifters of the MZIs are switched off or after a different obstacle/scattering medium is inserted in the system), the optical power measured at the output port of the left processor can be as low as -55 dBm ($>$ 70 dB loss). This power level is still above the sensitivity limit (-60 dBm) of the electronic controller described in Supplementary Sec. 2. From this initial condition the configuration algorithm automatically finds the best setting of the MZI processors to maximize the coupling strengths of the first two communication modes of the system. For instance, for the first mode, the power coupling measured at the output fiber is -20 dBm in the absence of obstacles, this corresponding to an overall loss of 35 dB (see Methods for the analysis of the system loss breakdown).

Supplementary Fig. 3b, instead, shows the schematic of the setup for the data transmission experiment illustrated in Fig. 4 of the main text. As it can be seen, the main difference with respect to the previous setup [panel a] is in the equipment used before and after the left and right photonic processors, respectively. A transceiver module is used to inject a 5 Gbps NRZ-OOK intensity-modulated signal into the system. After amplifying the signal using the same EDFA as before, a 50:50 fiber splitter is used to split the modulated signal into two branches. A coil of fiber is used in one of the branches for producing two decorrelated signals which both pass through in-line power meters (for adjusting the same power in the branches) and polarization controllers on each branch. The two fibers then are connected to a (multi-channel) fiber array which is mounted on a 6-axis stage for alignment on top of the $I/O_{1,2}$ linear array GCs of the left photonic processor, as shown in Supplementary Fig. 3e. On the right (Rx) side, instead, after the configuration of both processors as before, the upper (90%) branch of the fiber splitter is switched to another branch which consists of an EDFA (Amonics AEDFA-PA) followed by an ASE filter (JDS Uniphase TB9) and a variable optical attenuator to reach the power input levels needed for the oscilloscope (Tektronix) or for bit-error-ratio (BER) measurements, via connecting the fiber back to the Tx/Rx module. Note that the control electronics part of the setup, which is not depicted in panel b for simplicity, is the same as in the previous experiments done as in the previous setup of panel a.

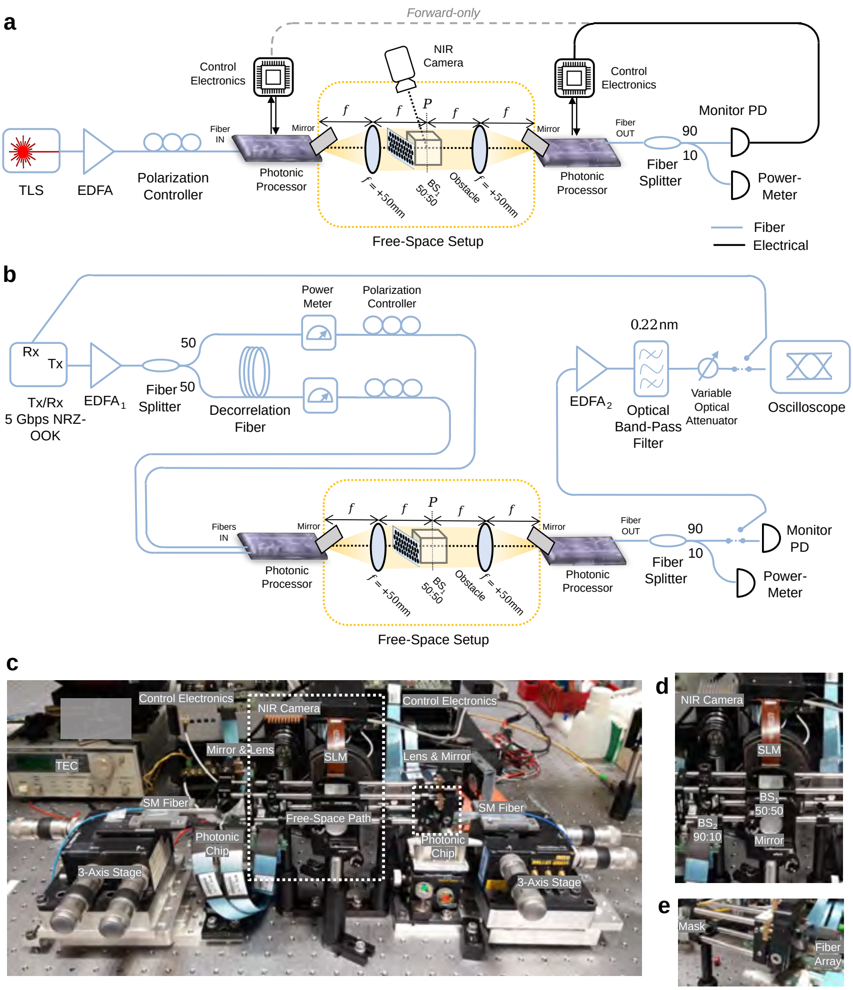

Fig. 3 Experimental setup. Schematic of the experimental setup showing the free-space optical system between the two photonic processors (orange dotted area), the fiber optics components employed at the input /output of the photonic chips (light blue lines), and the electrical circuit implementing the control algorithm (black lines). The setup schematic in panel **a** is used for the results shown in Figs. 1-3 of the main text, while the setup in **b** is used for the data transmission experiment of Fig. 4 of the main text. **c** Photograph of the chip-to-chip free-space system. The zoomed view on the right panel **d** shows the NIR camera and the reflective SLM coupled to the free-space path through beam splitters BS_1 and BS_2. Panel **e** shows a part of the laboratory setup with the fiber array and amplitude mask that is used for the transmission experiment of panel **b**.

Device	Layout	Characteristics
Waveguide and Thermo-Optic Phase Shifter (PS)		Insertion Loss: $\sim 1\ \mathrm{dB/cm}$ PS: TiN Metal Strips $(2\ \mu\mathrm{m}\ \times\ 80\ \mu\mathrm{m})$ Efficiency: $\sim 22\ \mathrm{mW}/\pi$ Time Response: $<\ 10\ \mu\mathrm{s}$
Mach-Zehnder Interferometer (MZI) with 2 PSs		Directional Coupler (DC) Gap: $300\ \mathrm{nm}$ DC Length: $40\ \mu\mathrm{m}$ MZI Extinction Ratio: $>35\ \mathrm{dB}$
Grating Coupler (Aperture)	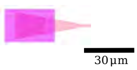	Transverse-Electric (TE) Polarization Beamwidth: $\mathrm{HPBW} \approx 5^\circ\ \times\ 9^\circ$ Tilt angle: 12° Size: $29.2\ \mu\mathrm{m}\ \times 19.3\ \mu\mathrm{m}$
Square Array of Apertures	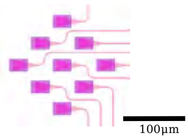	No. of elements: 9 Element Spacing: $50\ \mu\mathrm{m}$ Beamwidth: $\mathrm{HPBW} \approx 0.6^\circ\ \times 0.6^\circ$ Field-of-View: $\sim 1.7^\circ$

Fig. 4 Main building blocks used to implement the integrated photonic processors and their relevant characteristics. The technological platform is Silicon Photonics from the commercial foundry AMF (Singapore). A standard active Multiple Projects Wafer run has been used.

Supplementary Movie 1

Supplementary Movie 1 shows the camera view of the measured far field of the first (Mode 1, left) and second (Mode 2, right) modes during the automated setting performed by the two-processor system. The experimental conditions are the ones considered in Fig. 1f. “Reset” operations correspond to random settings of all the phase actuators of the two meshes, which are scrambled at each trial. In order to better appreciate mode evolution, the control algorithm is intentionally slowed down and is paused at each reset. Two modes are established sequentially (search for Mode 2 starts after convergence of Mode 1), however, for a better comparison the evolution of the two modes is shown together in the animation.

References

[1] Miller, D.A.B.: Establishing optimal wave communication channels automatically. J. Lightwave Technol. **31**(24), 3987–3994 (2013)

[2] Miller, D.A.B.: Self-configuring universal linear optical component. Photon. Res. **1**(1), 1–15 (2013). https://doi.org/10.1364/PRJ.1.000001

[3] Morichetti, F., Grillanda, S., Carminati, M., Ferrari, G., Sampietro, M., Strain, M.J., Sorel, M., Melloni, A.: Non-invasive on-chip light observation by contactless waveguide conductivity monitoring. IEEE Journal of Selected Topics in Quantum Electronics **20**(4), 292–301 (2014). https://doi.org/10.1109/JSTQE.2014.2300046

[4] Miller, D.A.B.: Self-aligning universal beam coupler. Opt. Express **21**(5), 6360–6370 (2013). https://doi.org/10.1364/OE.21.006360

[5] Zanetto, F., Grimaldi, V., Toso, F., Guglielmi, E., Milanizadeh, M., Aguiar, D., Moralis-Pegios, M., Pitris, S., Alexoudi, T., Morichetti, F., Melloni, A., Ferrari, G., Sampietro, M.: Dithering-based real-time control of cascaded silicon photonic devices by means of non-invasive detectors. IET Optoelectronics **15**(2), 111–120 (2021). https://doi.org/10.1049/ote2.12019

[6] Annoni, A., Guglielmi, E., Carminati, M., Ferrari, G., Sampietro, M., Miller, D.A., Melloni, A., Morichetti, F.: Unscrambling light—automatically undoing strong mixing between modes. Light: Science & Applications 2017 6:12 **6**, 17110–17110 (2017). https://doi.org/10.1038/lsa.2017.110